António José do Nascimento de Oliveira

Bachelor in Micro and Nanotechnologies Engineering

Dissertation for obtaining the degree of Master of Science in Micro and Nanotechnology Engineering

Nanoparticles in $Cu(In,Ga)Se_2$ thin film solar cells for light trapping

Supervisor: Doctor Pedro Salomé, Group Leader, International Iberian Nanotechnology Laboratory

Co-Supervisor: Doctor Manuel J. Mendes, Assistant Professor, Faculty of Sciences and Technology, New University Of Lisbon

Examination Committee:

Chairperson: Doctor Hugo Águas

Rapporteurs: Doctor Maria Correia
Doctor Pedro Salomé

FACULDADE DE CIÊNCIAS E TECNOLOGIA
UNIVERSIDADE NOVA DE LISBOA

November,2019

"If we knew what it was we were doing, it would not be called research, would it?"
Albert Einstein

Acknowledgments

This work was the culmination of the last 5 years. The path was hard but wasn't inconceivable due to the help that was given to me. Therefore, this section is reserved to thank everybody that has helped me throughout the course of this journey.

Gostaria em primeiro lugar de agradecer ao Prof. Dr. Rodrigo Martins e à Prof. Dr. Elvira Fortunato pela oportunidade que me foi concedida através da criação do curso de Engenharia em Micro e Nanotecnologias. Ademais, gostaria também de agradecer pela possibilidade de poder frequentar as instalações do CENIMAT|i3N e CEMOP desde cedo no curso.

Um agradecimento especial ao meu orientador, Prof. Dr. Pedro Salomé, sempre disponível e preocupado. Fui recebido de braços abertos e rapidamente informado e integrado nas atividades do grupo de trabalho no INL. É de salientar o esforço incansável do Pedro para o sucesso contínuo de todos os investigadores do grupo. Sempre que necessário esteve disponível para discutir resultados, para dar conselhos e apoiar. Todos os ensinamentos dados pelo "chefe" são de um valor incalculável, sendo que a realização deste trabalho não seria possível sem a sua ajuda.

Um muito obrigado ao meu co-orientador, Prof. Dr. Manuel Mendes. O meu interesse na área de células solares foi despertado pelas aulas do professor e por isso estou muito agradecido. Quero ainda agradecer por toda a ajuda e suporte durante os últimos meses.

Ao Prof. Dr. Paulo Fernandes deixo um agradecimento especial por todo o conhecimento e ajuda que me concedeu. Sempre que precisei o professor esteve disponível para ensinar e apoiar, e por isso muito obrigado.

A special thanks to all the INL staff that helped me throughout the course of this work, especially to Dr. Joana Guerreiro and Prof. Dr. Sara Abalde-Cela for all the help concerning the synthesis and deposition of the Au nanoparticles.

I want to thank all my colleagues and friends in the NOA group that helped me in this last months. Jennifer, Kevin, Marco, Miguel e Tomás quero agradecer muito pelos vossos ensinamentos, ajuda, e claro agradável companhia que muito facilitou a minha estadia no INL. Thank you, Olivier, for all of your patience during our SEM sessions and, of course, for all the advices and lessons. André, Célia e João muito obrigado pela companhia e ajuda nestes últimos meses. Thank you, Evelina and Ronja, for the good company and ping-pong competition during the "small" work breaks. Um agradecimento muito especial à chefona Beatriz que me aturou durante o início da minha estadia. Muito obrigado por toda a transmissão de conhecimentos e companhia. E claro um agradecimento muito especial ao meu companheiro de trabalho e colega de casa, Rodrigo, um muito obrigado pela paciência e disponibilidade sempre que precisei.

To all of the friends that I made in INL thank you for making my stay in Braga way less boring.

Deixo um agradecimento especial aos meus colegas de casa, Pedro, João, Rodrigo e Sara. A vossa paciência, suporte e companhia foi fundamental para superar esta etapa.

Quero agradecer aos meus colegas de curso que me acompanharam e apoiaram ao longo destes 5 anos. Deixo um agradecimento especial ao Matos, ao Bernardo e ao Chico.

Ao Modesto e ao Samuel por toda a companhia, camaradagem, ajuda e conselhos.

Um agradecimento muito especial à minha segunda família, os Morgado. Muito obrigado por me terem recebido de braços abertos e por todo o apoio que me dão.

Um muito obrigado ao meu irmão Ruben e à Andreia por terem sido a minha fonte constante de apoio e companhia.

Quero agradecer aos meus pais por me terem conferido todas as condições para poder chegar aonde cheguei hoje. Um muito obrigado por me terem permitido iniciar esta aventura.

Por último, quero deixar um agradecimento muito especial à Carolina. Não se pode descrever todo o amor, apoio e força que me deste durante o decorrer desta etapa. A tua ajuda foi fundamental para a realização deste trabalho.

Abstract

$Cu(In,Ga)Se_2$ (CIGS) solar cells have been receiving unique attention from the research and industry community, stemming mostly from the excellent electronic properties that allowed this technology to achieve record-breaking efficiency values (23.35%). However, CIGS contains scarce and expensive elements (In and Ga). Therefore, a continuous absorber layer thickness reduction is needed to allow for a large-scale deployment. However, as the absorber thickness decreases, insufficient light absorption is more evident. The work performed in this thesis tackles this topic and two novel light management architectures are studied and developed.

In the first approach, a broadband External Quantum Efficiency enhancement and a 3.28 mA/cm^2 short circuit current increase are obtained with the introduction of Au nanoparticle aggregates at the solar cell rear contact. This improvement might be attributed to two factors: the top surface roughness introduced by the Au aggregates and a rear contact diffuse reflection increase, as demonstrated through optical simulations.

The second approach consisted on optimizing the deposition of individual Au nanoparticles monolayers, to take advantage of the high scattering cross-section that the nanoparticles present at their resonant frequency. The deposition of individual nanoparticles with a minimal presence of aggregates is demonstrated.

Keywords: Solar cells, CIGS, light management, nanoparticles, Au

Resumo

As células solares de Cu(In,Ga)Se_2 (CIGS) têm recebido uma atenção especial por parte das comunidades científica e industrial. Tal se justifica maioritariamente devido às suas excelentes propriedades eletrónicas que permitem que se atinjam valores recorde de eficiência (23.35 %). Por outro lado, CIGS contem elementos escassos e dispendiosos (In e Ga). De modo a que esta tecnologia possa ser implementada em larga-escala, é necessária uma contínua diminuição da espessura da camada absorvente. No entanto, à medida que a espessura desta camada diminui, os problemas de absorção de luz tornam-se mais evidentes. Este estudo incide neste tópico, através do desenvolvimento de duas arquiteturas de manuseamento de luz.

Foi feita uma primeira abordagem, onde através da introdução de agregados de nanopartículas de Au no contacto traseiro da célula solar se verificou um aumento de banda larga da Eficiência Quântica Externa e um aumento de 3.28 mA/cm^2 da corrente de curto circuito. Tal pode ter sido resultado de dois fatores: devido à rugosidade da superfície frontal induzida pela implementação dos agregados e a um aumento da reflexão difusa do contacto traseiro, tal como foi demonstrado através de simulações óticas.

A segunda abordagem consistiu na otimização de um processo de deposição de uma monocamada de nanopartículas de Au individuais, com o intuito de aproveitar a grande secção-transversal de espalhamento de luz que estas nanopartículas apresentam na sua frequência de ressonância. Nesta abordagem, a deposição de nanopartículas individuais com uma presença mínima de agregados foi alcançada.

Palavras-chave: Células solares, CIGS, manuseamento de luz, nanopartículas, Au

Contents

List of figures

List of tables

Symbols

Symbol	Name	Unit
A	Ideality factor	
ABS	Total light absorption	%
Ag	Silver	
Al	Aluminium	
Al_2O_3	Aluminium Oxide	
$a\text{-}Si$	Amorphous Silicon	
Au	Gold	
c	Free space light speed	m/s
C	Concentration	M
Cd	Cadmium	
CdS	Cadmium Selenide	
Cu	Copper	
E	Electrical field	V/m
$\|E\|^2$	Electrical field intensity	V/m^2
FF	Fill-factor	%
Ga	Gallium	
h	Planck constant	J·s
$HAuCl_4$	Chloroauric acid	
$I_{AM1.5}$	AM 1.5 Intensity	$W/m^{2}{\cdot}m^{1}$
In	Indium	
J	Current density	A/m^2
j_0	Saturation current density	A/m^2
J_{ph}	Photogenerated current density	A/m^2
J_{SC}	Short-circuit current density	A/m^2
k	Extinction coefficient	
k_b	Boltzmann constant	$m^2{\cdot}kg{\cdot}s^{-2}{\cdot}K^{-1}$
L	Optical Path Length	cm
Mo	Molybdenum	
$MoSe_2$	Molybdenum Diselenide	
n	Refractive index	
N_2	Nitrogen	
N_2O	Nitrous Oxide	
NaF	Sodium Fluoride	
Ni	Nickel	
NP	Nanoparticle	
NPs	Nanoparticles	
P_{ABS}	Power absorbed per unit volume	W/m^3
p_{ABS}	Normalized power absorbed per unit volume	W/m^3
q	Electronic charge	C
C_{abs}	Absorption cross-section	m^2
C_{scat}	Scattering cross-section	m^2
r	Radius	m
R_p	Shunt resistance	Ω
R_s	Series resistance	Ω
Se	Selenium	
$SiH_{4\text{-}5}$	Silane	
Si_3N_4	Silicon Nitride	
SiO_2	Silicon Oxide	
V	Voltage	V
V_D	Applied voltage across the diode	V
V_{NP}	Volume of a Nanoparticle	m^3

V_{OC}	Open-circuit voltage	V
ZnO	Zinc Oxide	
α	Polarizability	$C \cdot m^2 \cdot V^{-1}$
λ	Wavelength	nm
ω	Angular frequency	rads/s
η	Power conversion efficiency	%
ε_0	Permittivity of vacuum	F/m
ε_m	Medium dielectric constant	F/m
ε''	Imaginary part of the dielectric permittivity	F/m
Φ	Photon flux	$s^{-1} \cdot m^{-2}$

Acronyms

AFM	Atomic Force Microscopy
Al:ZnO	Aluminium doped zinc oxide
APTMS	(3-Aminopropyl)trimethoxysilane
CBD	Chemical Bath Deposition
CGS	Copper Gallium Selenide
CIGS	Copper Indium Gallium Diselenide Cu(In,Ga)Se_2
CIS	Copper Indium Selenide
CGI	[Cu]/([Ga]+[In])
DC	Drop Casting
DWL	Direct Write Laser
EQE	External Quantum Efficiency
FDTD	Finite-Difference Time-Domain
FF	Fill Factor
GGI	[Ga]/([Ga]+[In])
HDMS	Hexamethyldisilizane
HF	High frequency
INL	International Iberian Nanotechnology Laboratory
i-ZnO	Intrinsic zinc oxide
LSP	Localized surface plasmon
MQ	Milli-Q Water
NP	Nanoparticle
NPs	Nanoparticles
PDDA	Poly(diallyldimethylammonium chloride)
PDMS	Polydimethylsiloxane
PECVD	Plasma Enhanced Chemical Vapor Deposition
PSS	Poly(styrenesulfonate)
PV	Photovoltaic
RIE	Reactive Ion Etching
RT	Room Temperature
SAM	Self-assembled monolayer
SCR	Space-Charge Region
SEM	Scanning Electron Microscopy
SLG	Soda lime glass
TCO	Transparent Conductive Oxide
TFSF	Total-Field Scattered-Field

Motivation and objectives

The technological advancements that are being experienced in this era have been contributing to a never stopping demand for energy. The majority of the produced energy has come from the burning of fossil fuels, such as, coal, petroleum and natural gas. The hazardous role that fossil fuels play on the environment, along with the inevitable depletion of these resources, demonstrates the necessity for the exploitation of "clean", renewable energy sources [1].

Amongst the renewable energy sources, solar power has gained a unique interest due to the inherent advantages associated with the harnessing of such energy. As it is known, solar energy is a never ending abundant clean energy source. With the Photovoltaic (PV) technology, e.g. solar cells, sunlight can be directly converted into electricity, without any direct green-house emission or noise [2]. However, for a worldwide deployment of this technology, progress towards the decrease of the cost of PV modules allied with the increase of the module's power conversion efficiency is required [3].

Thin-film solar cells have been the current research trend in solar cell technologies, as they allow the reduction of material consumption as well as the manufacturing cost of solar cell devices. CIGS solar cells stand out amongst the great variety of existing thin-film technologies, due to their excellent electronic properties, tolerance to environmental conditions and record-breaking efficiency values (23.35%) [1], [4], [5].

The presence of scarce and expensive elements such as indium and gallium in CIGS solar cells, may hinder the large-scale production of this technology [4]. For a continuous reduction of the consumption of these scarce elements and ultimately of the device cost, a further decrease of the absorber layer thickness is of outmost importance [1]. However, as the absorber thickness is decreased, problems like incomplete light absorption lead to the inevitable decrease of the solar cell short-circuit current (J_{sc}), and by association, a detriment on the device's performance. Therefore, light management techniques, that can range from the implementation of an anti-reflective layer to the employment of plasmonic nanoparticles (NPs) in the solar cell, can be used to mitigate the light's optical length inherent decrease with the reduction of the CIGS layer [1].

Light-management techniques are widely used in amorphous silicon, organic and even dye-sensitized solar cells, but only recently started to be investigated in CIGS solar cells [1]. Due to the different structure when compared with the aforementioned technologies, the direct transfer of the previously used light management concepts is not so simple [1]. Most publications concerning light management in CIGS technology approaches are only in a theoretical level. The main focus of this work tackles this topic, as novel light management techniques were studied and practically executed with the intent of maximizing the light's optical path and therefore the absorption in the ultra-thin CIGS layer.

The First approach was based on the use of Au nanoparticle (NP) aggregates at the rear contact of the solar cell. The utilization of such structures had the aim of exploiting the high diffuse reflection stemming from the roughness inherent to the Au NP aggregates. Furthermore, the conformal growth of the subsequent layers on top of the Au aggregates, is expected to create roughness on the solar cell's top layers, therefore leading to an increase of the front scattering of the incident light.

The second method consisted on the optimization of the deposition of individual plasmonic Au nanoparticles (NPs), to exploit the great scattering cross-section that these structures present at their plasmonic frequency.

1 Introduction

1.1 Solar cell electrical model

A solar cell is a device that utilizes the photovoltaic effect to convert light into electrical energy. A solar cell is typically composed by a p-n junction, where the p-type semiconductor is the absorber material. When a photon is incident upon the absorber material, if its energy is higher than the bandgap, then, an electron can be excited to the conduction band creating an electron-hole pair. However, the charge carriers can randomly encounter each other and recombine. Due to this, it is essential for the charge carriers to have a lifetime sufficiently long to be collected by the electrical contacts [6]. A p-n junction is used in a solar cell to facilitate the separation of the photogenerated carriers. The built-in electric field created by the combination of a p-type and n-type semiconductors, drives the charge carriers within the diffusion length region to be collected by their respective electrodes [7].

The Shockley model can accurately describe the current that passes through the junction, as it can be seen on **Equation 1.1** [8], [9]*:*

$$J = J_0\left(exp(\frac{qV}{Ak_bT}) - 1\right) \quad (1.1)$$

where V is the voltage applied across the diode, q is the electron charge, A the ideality factor, k_b the Boltzmann's constant, T the absolute Temperature, J the current density and J_0 the saturation current density. Under illumination, the current can be calculated through a superposition of the photogenerated current and the dark current that passes through the junction [10]:

$$J = J_0\left(exp(\frac{qV}{Ak_bT}) - 1\right) - J_{ph} \quad (1.2)$$

where J_{ph} is the photogenerated current. For a more accurate description, the equation can be modified to encompass ohmic and leakage current losses due to a series (R_s) and parallel (R_p) resistance [9]:

$$J = J_0\left(exp(\frac{qV - qJR_s}{Ak_bT}) - 1\right) + \frac{V - JR_s}{R_p} - J_{ph} \quad (1.3)$$

The single-diode model that can electrically represent a solar cell is demonstrated on **Figure 1.1 a).**

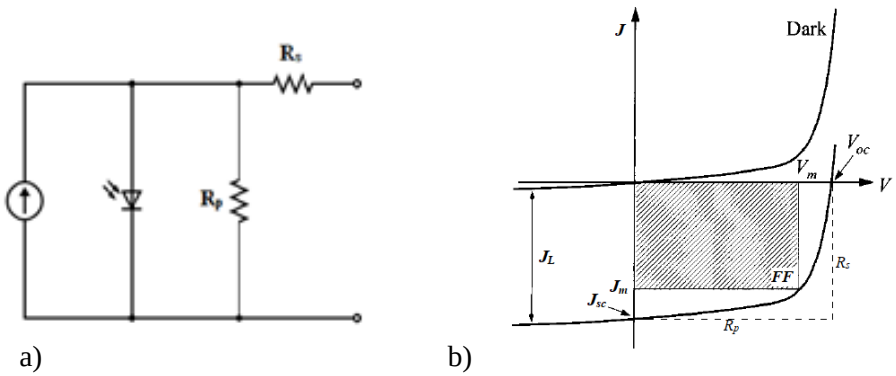

a) b)

Figure 1.1 - a) Single-diode model electrical representation, taken from [11]. b) J-V characteristics of a solar cell under illumination, adapted from [12].

The J-V characteristics of a solar cell under illumination, represented on **Figure 1.1 b)**, allow for the characterization of the device, since a great variety of parameters that describe the solar cell's performance can be extracted from it, such as, the open-circuit voltage (V_{oc}), the short-circuit current (J_{sc}), the Fill Factor (FF) and the conversion efficiency (n) [13].

The V_{oc} corresponds to the voltage value where the current density is zero, J_{sc} is the current density where there is no voltage across the junction, and the FF can be determined by:

$$FF = \frac{J_M \times V_M}{J_{sc} \times V_{oc}} \quad (1.4)$$

where J_M and V_M are the current and voltage that lead to the generation of maximum power. The conversion efficiency of light to electricity can be calculated through:

$$\eta = \frac{J_M \times V_M}{P_0} = \frac{J_{sc} \times V_{oc} \times FF}{P_0} \quad (1.5)$$

where P_o is the incident power in form of light.

The solar cell's performance can also be characterized through its EQE which is determined by the ratio between the number of carriers collected by the solar cell and the number of photons with a given energy incident on the device. Therefore, it considers the capability of the solar cell to convert the incident light into photogenerated current. It is useful since it allows the identification of losses at specific wavelength ranges that might be associated with fabrication properties of the devices [2], [8].

1.2 CIGS solar cell

There are two configurations that may exist in thin-film solar cells, they can either be in the substrate configuration (the light enters the solar cell through the top) or in the superstrate configuration (the light enters through the substrate) [14].

The typical structure for a CIGS solar cell is represented on **Figure 1.2.** The most common configuration is a substrate configuration, since in the superstrate configuration the interdiffusion of cadmium selenide (CdS) during the growth of the CIGS layer may lead to a decline of the solar cell's performance [14].

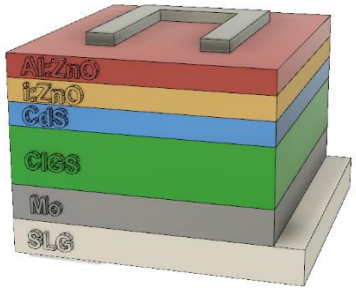

Figure 1.2 - CIGS solar cell typical structure.

1.2.1 Substrate and Rear Contact

Soda-lime glass (SLG) is the common chosen material for the substrate due to its abundance, low-cost, chemical inertness, thermal stability and to its thermal expansion coefficient which is similar to the CIGS coefficient [15]. The insulating behavior and smooth surface of the SLG also presents an advantage for a monolithic interconnection [15]. A great advantage of the SLG in a CIGS solar cell is the fact that it provides sodium to the absorber layer, it is known that the introduction of alkali-elements leads to an increase of the solar cell's performance [16], [17]. However, other strategies can be employed for the incorporation of the alkali elements inside the CIGS layer, such as, the deposition of alkali-containing compounds before, during or after the absorber layer growth [17].

As the contacting layer, molybdenum (Mo) is typically the material of election when it comes to CIGS solar cells. Properties like its chemical and mechanical stability, low diffusivity into semiconductor films and high melting point (~2700 ºC) make it able to withstand the harsh conditions during the absorber growth [18], [19]. Although Mo doesn't react with Ga, In or Cu, it reacts with Se to form $MoSe_2$. However, this layer allows for the formation of a quasi-ohmic-contact between CIGS and Mo [9], [15]. The drawback of the Mo is his low value of optical reflectivity. This property can be problematic when reducing the absorber thickness [20]. Mo is usually deposited by sputtering, and a two-step process is used to deposit a bilayer. Firstly, a higher pressure is used in order to obtain a good adhesion to the SLG substrate, then, a lower pressure is used to attain a layer with better conductivity [18].

1.2.2 Absorber layer

CIGS ($CuIn_{1-x}Ga_xSe_2$) is an I-III-VI semiconductor alloy that derives from CIS ($CuInSe_2$), through the replacement of some In atoms by Ga, thus belonging to the chalcogenide family. This compound crystallizes in a tetragonal chalcopyrite structure, as it can be represented in **Figure 1.3** [7], [14], [21].

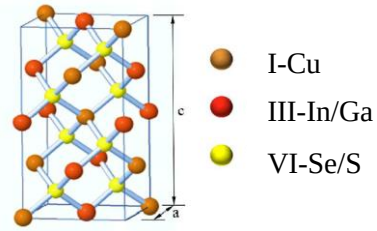

Figure 1.3 - CIGS's crystal structure.
Taken from [22].

CIGS presents a p-type conductivity, that stems from copper vacancies [9], therefore being an intrinsically doped material. This absorber has a direct bandgap and a very high absorption coefficient (~10^5 cm^{-1}), hence, a layer of about 2-3 µm is optically thick enough to fully absorb incoming photons [21]. Through the addition of Ga to the structure the bandgap can be engineered between the bandgap values of CIS (1.02 eV) and $CuGaSe_2$ (1.69 e V) [9]. Therefore, by controlling the [Ga]/[In] ratio, the bandgap can be tuned to match the solar spectrum [9], [18].

Various deposition methods can be used for the growth of the absorber layer, such as, co-evaporation, sputtering followed by selenization and sulfurization, electrodeposition or even printing. However only co-evaporated and sputtered CIGS films have led to high solar cell's efficiency values [15].

The Cu concentration in this quaternary compound is quite important since it may change significantly the properties of the semiconductor material. A compound is defined as Cu-rich if the [Cu]/([Ga]+[In]) (CGI) ratio is higher than 1 and it is defined as Cu-poor if the ratio is smaller than 1. A Cu-rich compound tends to form large grain sizes [23]. Even though this leads to superior crystalline properties, its electric properties would be far from ideal to use in this type of solar cell, since the semiconductor would have a lower p-type doping coming from the presence of less Cu vacancies [9], [23]. Although Cu-poor CIGS has worse crystalline properties, like small grains, its electrical properties are more adequate to be used in the solar cell [9],[23].

A Ga gradient can be implemented by varying the [Ga]/([Ga]+[In]) (GGI) ratio along the thickness of this layer. This gradient leads to the creation of a quasi-electric-field that repels the minority carriers from the rear contact, promoting a reduction of the rear-surface recombination and an increase in the effective diffusion length of the minority carriers, which results in improvements on the solar cell's figures of merit (V_{oc} and J_{sc}) [24].

1.2.3 Buffer and Window layers

To form the p-n-junction, the n-side of the junction is formed by the buffer layer. The most usual buffer layer is a thin (~50 – 70 nm) CdS layer deposited by chemical bath deposition (CBD). The use of CdS allows for an adequate band alignment between the window and absorber layer [15]. Furthermore, its refractive index has a value in between the ones of the absorber and window layer which leads to a minimization of the light's reflection [9]. Some authors even claim that the chemical deposition process leads to an improvement of the CdS/CIGS interface chemistry [14]. However, the relatively low bandgap (~2.4 eV) of CdS creates parasitic absorption for wavelengths of light below 515 nm. Besides that, the presence of Cd, a toxic element, serves as motivation to study alternative materials to use as buffers, such as (Zn,Mg)O or Zn(O,S,OH) [14], [15], [25].

The window is formed by a bilayer where both layers are usually deposited by sputtering. On top of the buffer layer a high-resistivity low roughness intrinsic ZnO layer (i-ZnO) is used to prevent shunts between the two contacts. The second layer works as the front contact. Ideally, for this purpose, it must have a high conductivity to collect the electrons and simultaneously a high transmission to let the light reach the absorber layer. Typically an aluminum doped zinc oxide (Al:ZnO) layer is used and a trade-off between the transparency and conductivity of the layer is achieved by the tuning of its thickness and its doping [9], [14], [21].

In the vast majority of cases, the cell is finished with a metallic grid composed of a stack of Ni/Al/Ni, that serves as a contacting pad to perform the solar cell characterization. Although the highly conductive grid facilitates the photogenerated current collection, the control of its design is crucial to the process. Afterall, it is an opaque material which blocks light, leading to a detriment of the

performance of the cell in an optical point of view. The role of the Ni layers is to prevent the formation of a resistive Al_2O_3 layer, by hindering the reactions of the Al with the front contact and air. The second Ni layer also eases the formation of an ohmic contact between the contact pad and the measuring probe [16],[26], [27].

1.3 State-of-the-art

The scientific community took their first interest on CIGS solar cells when an efficiency of 12% was achieved at Bell laboratories by S.Wagner *et al.* in 1975, when evaporating a thin layer of CdS on top of single crystal CIS. Boeing was the first company to obtain thin-film CIGS solar cells with an efficiency higher than 10 % by using a co-evaporation process to grow the absorber layer, where Cu, In and Se where originated from different sources. An efficiency of 12 % was achieved when using a thin CdS layer deposited by CBD. This became the typical process to be used for the deposition of the buffer layer [19]. From that point onwards, various technological advancements allowed the rise of the solar cell's efficiency values, such as, the incorporation of alkali elements into the absorber, doping CIS with Ga to become CIGS, or the use of a three stage co-evaporation process [18],[19]. As of the year 2019, the world record power conversion efficiency is at 23.35 % and it was achieved by Solar Frontier [5].

Currently, researchers are aware of the importance of developing ultra-thin (< 700 nm) CIGS solar cells. This can be justified because it will lead to a reduction of the material costs and of the processing time. Additionally, ultra-thin devices present lower bulk recombination values [20], [28], [29]. However, as the thickness of the absorber is decreased a higher density of charge carriers will be present at the interfaces, consequently, there will be an increase of the interface recombination rate. Moreover, the absorber thickness reduction will lead to incomplete light absorption. These problems are being tackled at this moment by various investigators, either through the passivation of both CIGS interfaces or by employing light management techniques [20], [28]. Such studies will be discussed later in **Sections 1.4** and **1.5.**

1.4 Passivation layer effect

The optical and electrical losses in ultra-thin devices can be tackled by the implementation of a passivation layer, typically an insulator between the CIGS/Mo interface. Usually a thin (~25 nm) sputtered Al_2O_3 layer is used to passivate the interface. However, other insulators have been subjects of study, such as, SiO_2, Si_3N_4, amongst others [28], [30]. Since Al_2O_3 is an insulator, electrical contacts need to be formed between the CIGS and the Mo layers. Various contacting approaches have been studied, however due to the short diffusion length of the carriers in CIGS, when designing such structures, the dimensions and the distance between the openings need to be taken into account [31], [32].

The introduction of this layer leads to two passivation mechanisms:

- Chemical passivation - The passivation layer is able to reduce the interface trap density, since it reduces the number of electronic active defects, such as dangling bonds, that otherwise would contribute to an increase on the rear surface recombination [28], [32].
- Field effect passivation - The high density of fixed charges present on the insulator, creates a built-in electric field. The latter is able to pull the minority carriers away from the rear contact, leading to a decrease on the back surface recombination [31], [32].

For certain dimensions, due to the refraction index of this layer, an increase in the rear optical reflection is verified. Therefore, an enhancement on the optical path of light occurs that may lead to an increase of the J_{sc} [32].

Salomé *et al.* demonstrated in [31] that the passivation through an 18 nm thick Al_2O_3 layer with nanopatterned point contacts, leads to an increase of the V_{oc} stemming from a decrease on the interface defect concentration. The studied structures also demonstrated J_{sc} improvements, which were attributed to both optical and electrical passivation effects.

1.5 Light management in CIGS solar cells

The major limitation of ultra-thin solar cells is the incomplete absorption of the incident light. This phenomenon is especially pronounced at higher wavelength values since the needed optical path for the light to be absorbed is significantly longer [29], [33]. **Figure 1.4** shows a plot of the percentage of light absorbed in a CIGS layer as a function of the absorber layer thickness. The absorption in the CIGS layer was estimated through the calculation of the material absorption coefficient for different wavelength values, and the used extinction coefficients (*k*) were extracted from [34]. As shown, with increasing wavelength the required thickness to absorb most of the incoming light is increasingly higher. To absorb most (>80%) of the incoming light in the IR range (700-1100) an absorber with a thickness higher than 500 nm is needed, a thickness as high as 3 µm is necessary for 1100 nm. Light trapping schemes are therefore essential to enhance the efficiency of ultra-thin solar cells by extending the optical light-path while keeping the absorber thickness thin. These light trapping schemes can be applied at both surfaces of the solar cell. Their integration can be done through many ways, with the intent of increasing the solar cell's efficiency, either by reducing the external reflection of light or increasing the internal light absorption. These designs have been the focus of investigation in thin film solar cells, since it allows them to be viable competitors to their bulk counter-parts [33], [35], [36].

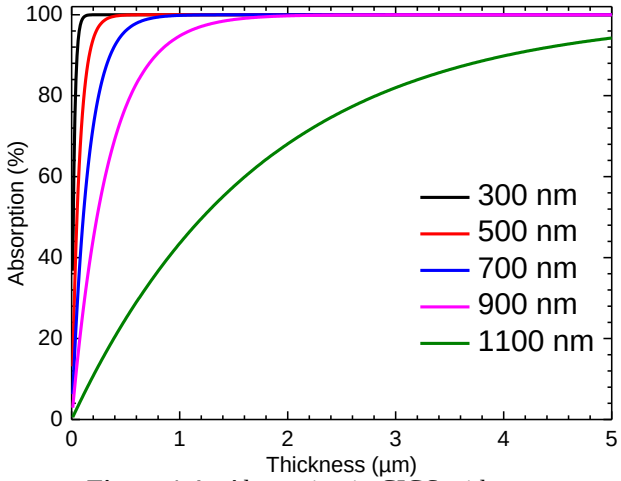

Figure 1.4 - Absorption in CIGS with respect to the layer thickness for various wavelength values.

As referred before, light management approaches have only recently started to attract attention in the CIGS technology, nonetheless some publications have already started to explore this field. The use of anti-reflection coatings has been widely studied, typically an MgF_2 layer with a refractive index of n = 1. 38 is used in order to minimize the reflection from the front contact [1]. Lopes *et al.* reported in [20] the use of a metal interlayer between the rear contact and an Al_2O_3 passivation layer, as a way to increase the rear optical reflection and consequently increase the optical path of light inside the absorber layer. Other approaches to further increase the localization of light inside the CIGS layer have been studied, such as the use of metallic nanoparticles, that at their surface plasmon resonance present a high scattering cross-section [1], [3], [4]. The main goal with the utilization of plasmonic NPs is usually to tune their plasmonic resonance to the IR range by changing the NPs size, shape and dielectric medium [1], [37]. The plasmonic NPs can be placed in either the front or back interface of the solar cell, however the placement of the NPs at the front surface can block the out-of-resonance light that otherwise would be absorbed by the solar cell. Therefore, it is more beneficial to place the NPs at the solar cell back contact, usually encapsulated in a dielectric material to red shift their plasmonic resonance [1], [37], [38]. This way, the NPs are able to interact only with the long wavelength light that isn't absorbed during the first pass in the solar cell, minimizing the parasitic optical losses [39]. Furthermore, a metallic layer can be place below the NPs, creating a so-called plasmonic back reflector, this way the light that reaches the back contact is scattered, either directly by the NPs or with the aid of the back reflector, at oblique angles that allow for an increase of the light's optical path in the absorber layer [38].

2 Materials and methods

The focus of this thesis consisted on the development of light management techniques with the use of Au NPs that would allow to mitigate the light absorption problems present in ultra-thin solar cells. In this chapter, all the development performed for the desired architectures is demonstrated as well as a summary of all the characterization techniques performed in this work.

2.1 Devices fabrication

In the scope of this thesis, two light management approaches were developed. The first approach was the use of Au NP aggregates while the second was the production of individual Au NPs monolayer. Therefore, for the different approaches, different NP sizes and different deposition methods were used. The choice of the Au material consisted on the fact that the synthesis protocol was already optimized by partnering groups at INL.

2.1.1 Gold nanoparticle synthesis

In this work, two Au NP synthesis were performed. The first synthesis was aimed to produce spherical particles with a radius of 12.5 nm. The experimental procedure for this synthesis was based on the work performed by Enüstün *et al*. [40]. First, 727.17 mL of a chloroauric acid ($HAuCl_4$) in milli-q water (MQ) solution, with a concentration of 0.25 mM, were heated under magnetic stirring. When the boiling point of the solution is reached (~70 ºC), 32.7 mL of a warm sodium citrate dihydrate ($HOC(COONa)(CH_2COONa)_2 \cdot 2H_2O$) solution (in MQ), at 65.3 mM were added. The final mixture was left under heating and constant stirring until it turned from a light yellow to a dark red color. The solution flask was then stored at 4 ºC covered with aluminum foil until further use. The final Au NP solution had a concentration of 0.12 mM, and the synthetized spherical particles an average radius of 12.3 nm, as measured through the analysis of the absorption spectrum of the solution and SEM images respectively. The solution's absorption spectrum and the determination of the solution's concentration and NP size is summarized in **Annex 1**.

The second synthesis was based on the work performed by Kenneth *et al*. [41], and the goal was to produce Au NPs with a radius between 50-70 nm. For that purpose, Au NP seeds with a smaller radius were firstly synthesized, through the same method utilized in the first synthesis. For the production of the seed solution, 125 mL of an aqueous $HAuCl_4$ solution with a concentration of 0.25 mM, were brought to boiling at constant magnetic stirring. After boiling, 12.5 mL of a warm aqueous solution of sodium citrate at 40 mM were added quickly. The final mixture was then left under heat and constant stirring until it turned to a dark red color. The seed NP solution was removed from heat and cooled down until it reached room temperature (RT). The growth of the Au seed particles was carried out at RT through the addition of 3 mL of an aqueous hydroxylamine-hydrochloride (NH_2OH:HCl) solution at 0.2 mM to 270 mL of a 0.25 mM aqueous solution of $HAuCl_4$, followed by the addition of 5 mL of the produced seed NP solution. The mixture was under constant stirring, and after a few minutes obtained a "turvy" brown color. The Au NPs were then functionalized through the addition of 1.7 mL of an aqueous sodium citrate dihydrate solution at 40 mM. The latter solution was then brought to the centrifuge at 4000 rpm for 5 min and re-dispersed in MQ. The final Au NP solution had a concentration of 0.14 mM, and the synthetized spherical particles an average radius of 59.12 nm, as measured through the analysis of the absorption spectrum of the solution and SEM images respectively. The solution's absorption spectrum and the determination of the solution's concentration and NP size is summarized in **Annex 1**.

2.1.2 Gold nanoparticles deposition methods

For the Au aggregate study, NPs with a 12.5 nm radius were deposited in substrates with three different top layers (Al_2O_3, Mo and SiO_2). Prior to the Au NP deposition, the substrates with a Al_2O_3 and Mo top layers were functionalized through a 1 min drop-casting (DC) with a 2% aqueous Poly(diallyldimethylammonium chloride) (PDDA) solution. While the substrates with a SiO_2 top layer were functionalized through two sequential DC procedures, the first is a 1 min DC with a 2 % aqueous Poly(styrenesulfonate) (PSS) solution, and the second is a 1 min DC in the PDDA solution. After the

functionalization step, the samples were dried with N_2 and placed in a petri dish. The Au NP deposition was then carried out through different methods (DC and immersion) and different times (1 h or 24 h).

For the monolayer study, the Au NP deposition was only carried out in one 2.5 x 2.5 cm SLG (3 mm) + Mo (350 nm) + Al_2O_3 (10 nm) substrate, since it is still in the optimization phase. Prior to the Au NP deposition the substrate was functionalized with (3-Aminopropyl)trimethoxysilane (APTMS). The silanization process for the substrate functionalization was conducted in the vapor phase. A drop of 97 % pure APTMS was deposited onto a glass slide and placed alongside with the sample in a desiccator. A vacuum environment was created inside the desiccator, which was then left at 65 ºC for 1 hour. This vapor phase method allows for the APTMS drop to evaporate and deposit in the sample leading to the formation of a self-assembled monolayer (SAM). For the Au NP deposition, microfluidic devices made of polydimethylsiloxane (PDMS), with a reservoir-like design were used. This deposition method was based on the work performed by Alexandra Teixeira *et al*. [42]. This method gives the ability to constrain the solution of NPs to a selected area and provides a better uniformity of the deposition. The PDMS reservoirs were fabricated using a mixture of PDMS and a cross-linker in a 10:1 ratio. This mixture was poured over a master mold provided by the Medical Devices group at INL. Using this mold allowed for the fabrication of reservoirs with a depth of 80 µm. The mixture was then degassed and cured at 65 ºC for 2 hours. The devices were then peeled-off from the master, and holes for tube connection were made. Prior to the Au NP deposition, the surface of the silanized sample and the PDMS device were submitted to an oxygen plasma treatment, to facilitate the adhesion of the device onto the substrate surface. The device was then bonded on top of the sample and taken to the oven for 10 min at 65 ºC. The Au NPs were then introduced onto the microfluidic structure through tubes, using a syringe. After 6 hours, the device was removed. An illustration of the Au NP deposition in the PDMS reservoir is represented in **Figure 6.2** in **Annex 2**.

2.1.3 Solar cell fabrication

For the solar cell fabrication only the substrates that are englobed onto the Au NP aggregates study are considered in this section, since the monolayer study is still currently under optimization.

The substrate preparation started at Uppsala University, where a 350 nm Mo layer was deposited through Direct Current sputtering on top of 5x5 cm SLG substrates. The samples were then shipped to INL, for the preparation of the rear structure. Prior to any depositions, the substrates were submitted to a standardized cleaning protocol with acetone, isopropanol and di-ionized water.

Before the absorber layer deposition, the solar cell's rear structure was prepared at INL. For simplicity, a summary of the samples structure prior to the absorber deposition and a step by step schematic of the rear structure fabrication are represented on **Table 2.1** and **Figure 2.1**, respectively. For the solar cell fabrication, eight samples were prepared: two reference samples without passivation or NPs, two passivated samples with a dielectric layer deposited and patterned on top of the Mo layer (ALPASS and SIPASS) and four samples with Au NP aggregates (AL, MOAL, SI and MOSI) with different structures that will be explained more in detail in **Section 3.3.1**.

Table 2.1 - Structure of the samples prior to the absorber deposition.

Sample	Structure
REFERENCES	SLG (1mm)/Mo (350 nm)
ALPASS	SLG (1mm)/Mo (350 nm)/Al_2O_3 (25 nm)
SIPASS	SLG (1mm)/Mo (350 nm)/ SiO_2 (30 nm)
AL	SLG (1mm)/Mo (350 nm)/Al_2O_3 (10 nm)/Au agregates/Al_2O_3 (15 nm)
MOAL	SLG (1mm)/Mo (350 nm)/Au agregates/Al_2O_3 (25 nm)
SI	SLG (1mm)/Mo (350 nm)/SiO_2 (20 nm) Au agregates/SiO_2 (10 nm)
MOSI	SLG (1mm)/Mo (350 nm)/Au agregates/SiO_2 (30 nm)

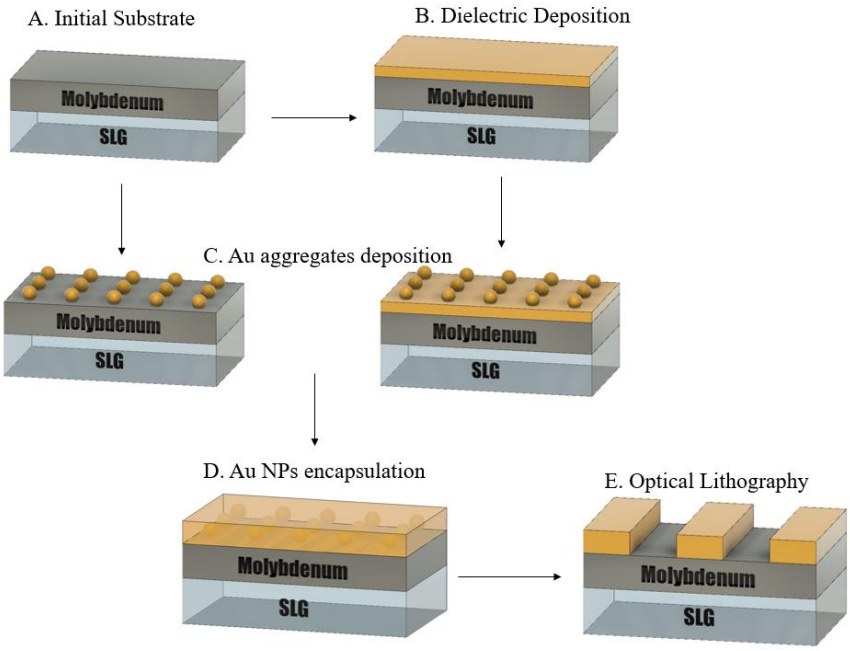

Figure 2.1 - Step by step schematic of the sample preparation prior to the absorber deposition.

In some of the developed samples, prior to the Au NP deposition, as represented on **Figure 2.1**, either a 10 nm Al_2O_3 layer (AL) or a 20 nm SiO_2 layer were deposited (SI). The Au NP deposition for each substrate was optimized, as it is explained on **Section 3.3.1**, and the Au NPs were deposited in concordance to the methods referred in **Section 2.1.2**, in samples AL, MOAL, SI and MOSI. For the deposition of the passivation/encapsulation layer, an Al_2O_3 layer was deposited in samples AL, MOAL and ALPASS in order to complete a 25 nm Al_2O_3 layer. While in samples SI, MOSI and SIPASS a SiO_2 layer was deposited to make up a thickness of 30 nm. The Al_2O_3 depositions were performed through Radio Frequency sputtering using a Metallization Singulus Sputtering tool (Timaris FTM). The argon injection flow in the camera was at 200 sccm and the utilized source power at 1500 W. During this process, due to the substrate proximity to the Al_2O_3 target, the substrate can reach temperatures of 200 ºC. The SiO_2 depositions were conducted through Plasma Enhanced Chemical Vapor deposition (PECVD), using the SPTSMPX CVD tool at 300 ºC, at High Frequency (HF) conditions, the precursor gases were SiH_{4-5}, N_2 and N_2O and the plasma power was at 30 W.

After the dielectric deposition, the line contact pattern was produced through optical lithography. The desired pattern consisted on trenches with 700 nm with an inter-distance of 2 µm (pitch). The lithographic process started with a hexamethyldisilizane (HDMS) vapor priming process to facilitate the resist adhesion. The samples were then coated with a 600 nm AZ1505 resist layer using the Karl Suss Optical Track system. The samples were then exposed through Direct Write Laser (DWL system, DWL 200). The development with AZ400k was performed on the Suss optical track through spin-coating. To create the trenches the samples were then submitted to a reactive ion etching (RIE) process recurring to a STPS ICP tool. The tool relies on the use of chlorine ions to etch the materials which may cause contaminations on the sample. Therefore, after the etching process the samples were rinsed with di-ionized water. The etching time was 45 seconds for samples AL, MOAL and ALPASS, and 20 seconds for samples SI, MOSI and SIPASS. Finally, the unexposed resist was stripped in a 20 min ultrasonic bath in acetone.

To complete the fabrication of the final device, all the samples were shipped to imec. The structure fabricated at imec, after the rear structure preparation, was the same for every sample and it is as follows: NaF (7 nm)/CIGS (500 nm)/CdS (50 nm) /i:ZnO (100 nm)/Al:ZnO (400 nm)/ Ni\Ag\Ni metallic grid. The NaF layer was deposited trough co-evaporation. The absorber CIGS layer was deposited through a one stage co-evaporation process at a temperature of 550 ºC. Since a one-stage process was done, there is no Ga gradient in the produced samples. The Cds layer was deposited through CBD. The i:ZnO and Al:ZnO layers through sputtering. Finally, the metallic grid was deposited through

e-beam deposition.

Despite the preparation of 8 samples, only 7 sets of solar cells were made, since sample AL broke during transportation to imec. Each sample contains 32 solar cells with a 0.5 cm^2 area that were defined through mechanical scribing.

2.2 Characterization techniques

During the development of this work various characterization techniques were used in different stages of the experimental procedure, which are summarized in this section.

The optical absorption and reflection measurements were performed with the Perkin-Elmer Lambda 950 UV-VIS-NIR spectrophotometer tool. This technique was used to produce the absorption spectrum of the Au NP solutions, from both performed synthesis. With the aid of an integrating sphere, the relative total and diffuse reflection of all the samples performed in the Au aggregate study were measured. These measurements were performed in various stages both during the optimization and in the device fabrication stage.

Scanning Electron Microscopy (SEM) images were taken with the use of a NovaNanoSEM650 system to perform a surface analysis at different stages of the work.

Atomic Force Microscopy (AFM) morphological analysis were also performed in the Au aggregate study. The measurements were performed on tapping mode with a scan rate of 1 Hz recurring to the AFM Dimension Icon System.

The electrical characterization of the solar cells produced in this work was conducted through two techniques: J-V and EQE measurements.

The J-V analysis was conducted with a home-made system. In the system setup, the cells are illuminated with an Oriel LSH-7320 ABA LED Solar Simulator, which was calibrated to a 1kW/m^2 intensity, with the help of a PV reference cell (PN 90034568). A source meter (Keithley 2420) was used to apply a voltage range from -0.5 V to 0.8 V, with a step of 1 mV. The current flow through the solar cell was limited to 40 mA/cm^2.

The EQE measurements were performed with a solar cell efficiency measurement system QEX10. These measurements were performed in a wavelength interval of 300 nm to 1100 nm with a 10 nm step.

For the Optical simulations performed in this thesis, the finite-difference time domain (FDTD) solutions package from the commercial Lumerical software was used. The FDTD method allows direct time and space solutions to the Maxwell's equations. A frequency solution can also be obtained through this method using Fourier transforms, allowing for the calculation of reflected or transmitted light [43].

Two different simulation setups were used. For the optical simulation of the solar cell's performance (**Sections 3.1** and **3.3.2**), a 2 µm FDTD region with symmetric and anti-symmetric boundary conditions was used to reduce the simulation time and memory usage. A broadband plane wave source was used to simulate the solar illumination. A wavelength interval of 300 nm to 1100 nm was chosen to match the EQE measurements. The optical properties of the chosen materials, mainly their complex refractive index (n,k), will define the outcome of the performed simulations. The complex refractive index values for: the Al:ZnO layer was taken from [44], the i:ZnO layer from [45], the Cds layer from [44], for the CIGS layer with a GGI = 0.30 from [34], for the Al_2O_3 layer from [46], for the SiO_2 layer from [46], for the Au material from [47] and for the Mo layer from [48].

The Au NP optical behaviour simulation performed in **Section 3.2** was based on the Mie Scattering 3D set available on Lumerical application gallery [49]. For this simulation setup, a Total-field scattered-field (TFSF) source was used with a bandwidth of 300-1100 nm. The TFSF source is used here to study the scattering behaviour of the simulated Au NP since it can separate the scattered field from the incident field [43]. The Au NP material complex refractive index was again taken from [47].

3 Results and discussion

In this chapter all the results obtained in the scope of this work are demonstrated and discussed.

Section 3.1 includes the optical simulations demonstrating the importance of implementing light management architectures.

In **Section 3.2** an optical study of Au NPs is performed. The optical simulations performed in this section were utilized to decide the radius of the Au NPs used for each approach.

In **Section 3.3** all the results from the first light management approach are demonstrated, from the optimization stage to the optoelectronic characterization of the final device.

In **Section 3.4** the results obtained for the development of the second light management approach are shown.

3.1 Importance of light management in CIGS

The decrease of the CIGS solar cell's absorber thickness is a necessity in an industrial point of view as it would allow for a reduction of the material cost and an increase of the machine throughput [4]. However, many issues arise with this, mainly the incomplete light absorption as the thickness decreases. The ultra-thin device's potential can be optimized with the implementation of light management techniques that allow for the increase in the light's optical path inside the absorber layer [3]. In this section, optical simulations were carried out that demonstrate the need to implement innovative light management techniques that would allow the CIGS ultra-thin solar cells to reach the performance achieved by their thick counterparts.

3.1.1 Numerical Model

A solar cell stack can be optically characterized through the FDTD solutions package from the commercial software Lumerical. In this analysis, the total light absorption (*ABS(λ)*) in each layer and the J_{sc} in the absorber layer can be calculated. First, through the electric field distribution in each region, the power absorbed per unit volume (P_{ABS}) can be calculated in each layer:

$$P_{ABS} = \frac{1}{2}\omega\varepsilon''|E(\lambda)|^2 \quad (3.1)$$

where, λ is the wavelength, $|E|^2$ is the electric field intensity, ϵ'' is the imaginary part of the dielectric permittivity and ω is the light angular frequency. In order to obtain the *ABS(λ)* in each layer, P_{ABS} needs to be normalized by the source power, the total light absorption can then be calculated through the integration of the normalized power (*pABS*) over a specific volume:

$$ABS(\lambda) = \int p_{ABS} dV \quad (3.2)$$

To determine the solar cell's J_{sc}, it is assumed that the internal quantum efficiency of the solar cell stack is 1 (e.g. every absorbed photon in the CIGS layer generates charge carriers that will be collected by the electrical contacts). Therefore, J_{sc} is estimated through the following integration [50]:

$$J_{sc} = q\int \frac{\lambda}{hc} ABS(\lambda) I_{AM\ 1.5}(\lambda)\, d\lambda \quad (3.3)$$

where, $I_{AM\ 1.5}$ is the source irradiance spectrum, c is the speed of light in vacuum and h is the Planck constant. As previously referred, every photon that is absorbed in the CIGS layer leads to the generation of an electron-hole pair. Therefore, the calculated J_{sc} only considers the optical behavior of the layers in the solar cell stack and does not encompass any electrical losses [50].

The simulations accuracy is tested by comparing the simulated solar cell stack absorbed light with the calculated absorbed light from Lumerical's Transfer Matrix analytical formalism. The performed accuracy test is represented on **Figure 6.3 (Annex 2)** (for simplicity reasons only one test is demonstrated). All the simulated structures in this section demonstrated a good overlap between the simulated and analytical results.

3.1.2 Optical simulations

Three different structures are compared in this section: a conventional CIGS solar cell with an absorber thickness of 2 µm, an ultra-thin CIGS solar cell with an absorber layer of 500 nm and an ultra-thin solar cell coupled with a near-perfect rear reflector, a so called "optical mirror" (Al_2O_3 (25 nm) + Au stack (20 nm)) at the absorber rear surface. The base structure of the simulated cells are as follows: Mo (350 nm)/ CIGS/ CdS (50 nm)/ i:ZnO (100 nm)/ Al:ZnO (400 nm).

The simulated absorption both in the CIGS layer and substrate are represented on **Figure 3.1. a)** and the solar cell's total reflection on **Figure 3.1. b)**. The conventional solar cell J_{sc} (30.29 mA/cm^2) is much higher than the J_{sc} (27.39 mA/cm^2) from its ultra-thin counterpart. This 2.9 mA/cm^2 difference stems from the decrease in light absorption as the absorber thickness is reduced and it happens mostly in the long wavelength region (>800 nm). The decrease in absorption is more pronounced at near-bandgap wavelength values (1100 nm) and it becomes increasingly lower as the wavelength is decreased, this result is shown on **Figure 3.1. (a)** and it is in accordance with results demonstrated in previous works [1], [20]. The incomplete absorption in the ultra-thin device is evident in the simulated parasitic absorption on the device rear structure (Mo+Al_2O_3+Au), which is directly correlated to the light transmitted from the absorber layer. Just by decreasing the absorber's thickness, an increase on the substrate's parasitic absorption of almost 30% (abs) occurs at 1100 nm. When the optical mirror is added to the ultra-thin device a J_{sc} current of 28.69 mA/cm^2 is obtained. By adding a highly reflective material such as Au, a great decrease in the substrate's parasitic absorption is clearly demonstrated, as well as an increase in the solar cell's total reflection. These results clearly imply that the introduction of the "optical mirror" leads to an increase of the absorber's rear surface total reflection, allowing for a second pass of the light in the absorber layer. The improvements demonstrated in this simulation are in accordance with simulation results obtained by Lopes *et al*. [20], where the implementation of different metals in CIGS solar cell clearly lead to an enhancement of the devices J_{sc}.

With only the integration of the "optical mirror", the absorption observed in the conventional device is still not reached, especially in the IR range (700-110 nm). For wavelength values higher than 950 nm the optimized device reflection is much higher than the conventional thick solar cell, suggesting that a great percentage of the light is exiting the solar cell and not being absorbed in the second pass. Thus, explaining the high J_{sc} difference between the optimized device and the thick reference cell. Therefore, the employment of light management architectures that allow further increases in the light's optical path inside the CIGS layer are needed to further approach the performance of thick conventional devices. In this work, two novel light management approaches in CIGS devices that tackle the enunciated problem will be explored.

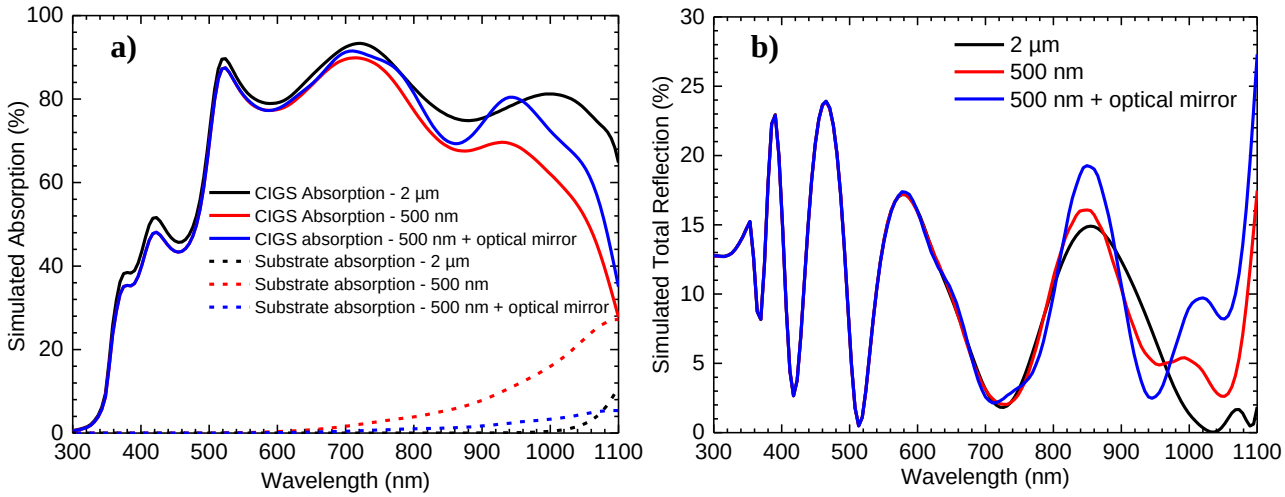

Figure 3.1 - a) Simulated absorption in the CIGS (solid lines) and substrate (dashed lines); b) Simulated total reflection.

3.2 Determination of the NP size

As referred before, two major approaches were tackled in this work as light management alternatives in CIGS devices. The first approach was the utilization of Au NP aggregates, in order to exploit their intrinsic roughness and the roughness that they will create on the subsequent layers. Hence, an increase of the light's diffuse scattering at the rear interface as well as in the other surfaces is expected. The second method consisted on the optimization on the deposition of a monolayer of individual Au NPs, that will ultimately be implemented in the rear substrate of an ultra-thin device to utilize the high scattering cross-section of the NPs in their resonance frequency. However different NP sizes are required for the different approaches. Therefore, optical simulations of the NPs scattering and absorption cross-sections were performed in order to determine which size is more appropriate to be used in each study.

3.2.1 Numerical Model

The Numerical Model used in this section was based on the Mie Scattering 3D set present on Lumerical application gallery [49]. As explained in **Section 2.2** this model recurs to a TFSF light source that surrounds the NP. The area inside this type of source englobes the existent total-field whereas the area outside encompasses only the scattered field by the NP. To calculate the net power absorbed by the NP (P_{abs}), an analysis group inside the TFSF source is utilized. Whereas, an analysis group located outside the TFSF source is utilized to calculate the net power scattered from the NP (P_{scat}). Both net powers can be calculated through **Equation 3.1**.

The scattering (C_{scat}) and absorption (C_{abs}) cross-sections are then calculated by normalizing the corresponding net power to the source intensity.

$$C_X = \frac{P_X}{I_{AM\ 1.5}} \tag{3.4}$$

The scattering and absorption cross-sections are then normalized to the NP volume to calculate the corresponding MIE efficiency.

The performed simulations were carried out assuming a uniform medium with a refraction index of 1 (e.g. air).

The accuracy of the simulations is then tested by comparing the obtained results with the theoretical results computed using the Au optical data, as represented on **Figure 6.4** in **Annex 2** (for simplicity, only one plot is shown, since all the performed simulations presented a good overlap between the simulated results and the analytical solutions).

3.2.2 Optical simulations

When the frequency of an incident photon is in resonance with the collective oscillations of the free electrons present in the NP, a phenomenon called localized surface plasmon (LSP) resonance occurs at a certain frequency [51]. In this situation, the resonant electron oscillations induce an electric field in the NP than can be much larger than the incident electric field. The generated electric fields can lead to a strong scattering and/or absorption behavior from the nanostructure, depending on various factors, such as, the nanostructure size, shape, dielectric medium, amongst others [51], [52]. The study of the NP absorption and scattering efficiency is crucial to understand which NP size should be used for each application studied in this work.

In this series of simulations, NPs with a radius (r) ranging from 12.5 nm to 100 nm were studied, and their corresponding MIE scattering and absorption efficiency values are represented on **Figures 3.2. a)** and **b)**, respectively. For a $r \leq 50$ nm, it is shown that with an increase in the NP size there is a redshift of both the absorption and scattering efficiency values as well as an increase in both quantities. This increase is more pronounced in the scattering efficiency than in the absorption efficiency. It is also demonstrated that for smaller radius the absorption efficiency is dominant over the scattering efficiency. This effect is mitigated as the NP size is increased. The obtain results for $r \leq 50$ nm are well explained by utilizing a quasi-static approximation of the electromagnetic field inside the NP: the electromagnetic field is constant inside the nanostructure. In this case, a dipolar approximation can be used, meaning that the interaction between the electromagnetic field and the NP is only governed by dipole oscillations [51]. The polarizability (α) of a sphere, which determines the degree at which the incident

electromagnetic field is enhanced in the NP [53], is calculated through the Clausius-Mossotti relation [51]:

$$\alpha = 4\pi\varepsilon_0 r^3 \left(\frac{\varepsilon - \varepsilon_m}{\varepsilon + 2\varepsilon_m}\right) \quad (3.5)$$

where ε_m is the dieletric constant of the surrounding medium, ε is the NP dielectric function and ε_0 is the permittivity of vacuum. The scattering and absorption cross-sections (C_{scat} and C_{abs}) are depended on the polarizability and can be calculated as follows [54]:

$$C_{scat} = \frac{1}{6\pi}\left(\frac{2\pi}{\lambda}\right)^4 |\alpha|^2 \quad (3.6)$$

$$C_{abs} = \frac{2\pi}{\lambda} Im|\alpha| \quad (3.7)$$

As the NP is illuminated, the light's electric field forces the conduction electrons to the surface. Since the electrons are confined to the NP, positive charges will be accumulated in the opposite side of the NP, therefore creating an electric dipole. An electric field is then created inside the NP that forces the electrons back to the equilibrium position [52]. The displacement of electronic charges will then induce an oscillatory behavior similar to a linear oscillator. The charges will then keep oscillating with a certain frequency (resonant frequency). As the Au NP size increases, the generated oscillations will occur with a lower frequency (higher wavelength), thus explaining the observed red-shift in the results [51]. The verified intensity increase is related to the scattering of the oscillating electrons with the NP surface. As the NP size increases, the portion of electrons close to the NP surface will decrease leading, therefore, to a decrease of the scattering resultant damping of the intensity [52]. According to the equations presented above, the increase in the scattering efficiency should be more pronounced then in the absorption efficiency, due to the dependency of both quantities on the NP radius. As the volume increases the scattering and absorption cross-sections will correspondingly scale with the 6th and 3rd power of the NP radius [55]. The theoretically expected increase corresponds well with the simulated results, as the increase seen in the scattering efficiency peak, when going from a NP with 25 nm radius to 50 nm radius is much higher than the increase observed in the absorption peak.

For $r > 50$ nm, the NP cannot be considered much smaller than the wavelength of light, and therefore the dipolar approximation is not sufficient to analyze the structure's optical behavior [52]. Since the electromagnetic field is not constant inside the NP, other resonant modes can appear. The variation of the scattering and absorption cross-sections stops being as linear as described before. For the scattering behavior, the main peak keeps red shifting and increasing. However, the increase is not as pronounced as before. The results from the absorption cross section are different, as the radius surpasses 50 nm a dampening of the absorption efficiency occurs and the main peak blue-shifts. These effects are related to the formation of other resonant modes inside the NP and are in good agreement with the results obtained by Garcia *et al.* [52]. Since the ultimate goal of this section isn't an in-depth study of the NP optical behavior, the reader is directed to other works for more information [51], [52], [55], [56].

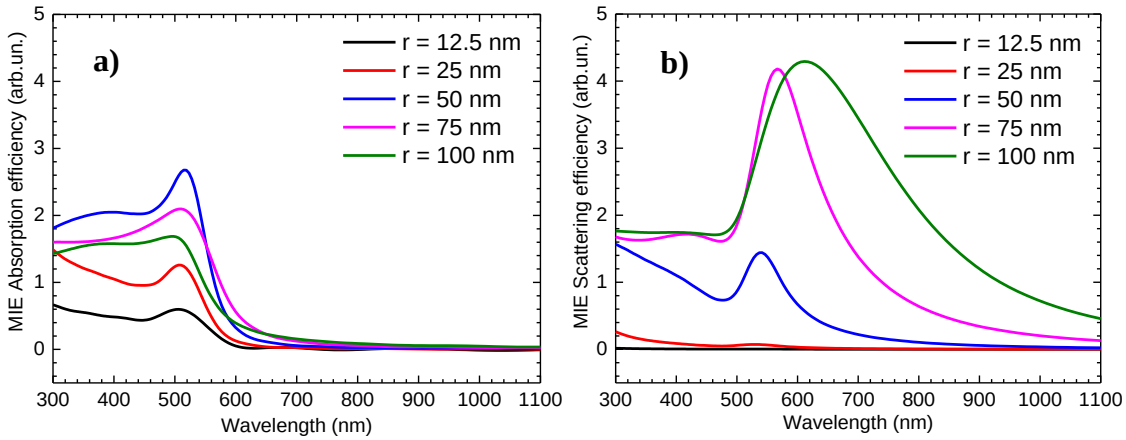

Figure 3.2 - a) Simulated MIE absorption efficiency; b) Simulated MIE scattering efficiency.

For the individual monolayer study, it is important to employ NPs with a high scattering efficiency at longer wavelength values, in which the light's absorption is harder. It might seem that the results obtained in theses simulations for any NP size demonstrate that there wouldn't be any significant scattering at long wavelength values. However, the simulations were performed in a surrounding air medium which has a low dielectric function, and the main goal is to encapsulate the deposited NPs in a dielectric medium that can also be used as the solar cell's passivation layer. As it is shown from **Equation 3.5** the resonant behavior, which occurs at $\varepsilon = -2\varepsilon_m$, is dependent on ε_m, and it will occur at longer wavelength values with the increase of this parameter [38], [55], [56]. Furthermore, the interaction between neighboring NPs is not being considered in the performed simulations which can have effects on the scattering spectrum [57].

Considering the obtained results and the structural limitations of the quaternary material that composes the absorber layer. In order to facilitate the absorber growth, it was decided to use the smaller NP radius (12.5 nm) for the aggregate's deposition study. NPs with a 12.5 nm radius, despite having the lowest MIE scattering efficiency, were chosen for this study since the goal is not to exploit the plasmonic effects of the aggregate structures, but the scattered light provided just by the structure in a photonic point of view. Whereas, for the individual monolayer, it was decided to use NPs with a radius between 50-70 nm, which have a considerable scattering behavior at their plasmonic resonance. Furthermore, the chosen NPs have an adequate size to facilitate the absorber deposition.

3.3 Light management through Au nanoparticle aggregates

In the following section, all the experimental procedures performed for the study of the influence of the Au NP aggregates on the solar cell's performance are summarized. **Section 3.3.1** entails the development of the deposition methods of the Au NP aggregates in different substrates as well as the substrate preparation to produce the final devices. In **Section 3.3.2** optical simulations of the final device structures are performed with the commercial Lumerical software. Finally, in **Section 3.3.3** the characterization of the final solar cell devices is represented.

3.3.1 Substrate preparation

The main goal of this study was to verify how the scattering, provided by NP aggregates as well as by the roughness that those aggregates induce on the subsequent layers, influence the solar cell's performance. For such purpose, the deposition of Au NP aggregates was studied in three different top layers (Al_2O_3, SiO_2 and Mo).

As referred in **Section 2** of this thesis, for the Au NPs deposition, a functionalization of the studied substrates was performed to allow the adherence of the Au NPs to the studied layers. For this purpose, two polymers were used (PDDA and PSS).

PDDA is an organic polymer that presents a strong adsorption in a great variety of substrates, the polymer's structure is represented in **Figure 3.3**. This effect occurs due to a strong electrostatic interaction between its charged quaternary ammonium group and the negatively charged substrate. Due to the stabilizing agent (sodium citrate) used during the NP synthesis, which promotes an overall negative charge on the nanoparticle's surface, the same interaction will occur between the Au NPs and the remaining ammonium groups [58]. The functionalization with PDDA was studied before the start of this study and it was successful for the deposition in Al_2O_3 and Mo layers. However, for SiO_2 layers it was discovered by Cunha *et al*. [30] that in the SiO_2 deposited through PECVD in HF conditions at 300ºC, the fixed insulator charges of the layer show an overall positive polarity. Hence, a two-step functionalization was performed in these substrates in order to allow for the Au NPs adhesion. Before the PDDA deposition, a functionalization with PSS, where the sulfoxide group provides the polymer with an overall negative charge, was performed. This way, a polymer double-layer is created, in which the negatively charged PSS will interact with the substrate and the positively charged PDDA with the Au NPs.

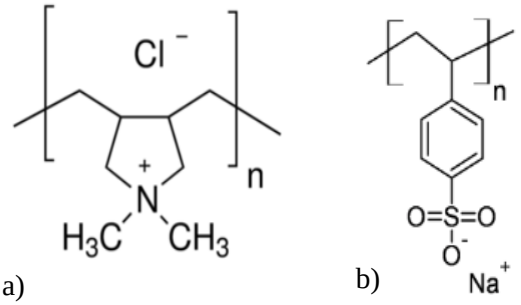

Figure 3.3 - Chemical structure of PDDA (a) and PSS (b), Taken respectively from [59], [60].

In order to determine the best deposition conditions for each substrate, ten SLG (3 mm) + Mo (350 nm) 2.5x2.5 cm substrates were used. A 10 nm Al_2O_3 layer was deposited on 4 samples (AL X) and a 20 nm SiO_2 layer on other four (SI X), while in the remaining two no layer was deposited (MO X). This way, the Au NP deposition in different layers can be studied. Various tests were performed where the Au NP deposition method was varied, as well as the contact time between the Au NP solution and the substrate. The full list of experiments is represented on **Tables 3.1**, **3.2**, and **3.3**. It is important to note that in the samples with no dielectric top layer (MO 1 and MO 2), the Au NP deposition was only performed for 1 hour. This is due to the fact that in a previous study conducted by the group, it has been verified that a long contact time between the Au NP solution with the Mo layer leads to the formation of cracks. The formation of these aberrations was then attributed to the acidic nature of the Au NP solution.

Table 3.1 - Series of experiments performed on the substrates with an Al_2O_3 top layer.

Sample	Structure	Functionalization	NPs deposition
AL 1	SLG (1 mm) + Mo (350 nm) + Al_2O_3 (10 nm)	Drop-Casting in PDDA (1 min)	Immersion 24 h
AL 2	SLG (1 mm) + Mo (350 nm) + Al_2O_3 (10 nm)	Drop-Casting in PDDA (1 min)	Immersion 1 h
AL 3	SLG (1 mm) + Mo (350 nm) + Al_2O_3 (10 nm)	Drop-Casting in PDDA (1 min)	Drop-Casting 24 h
AL 4	SLG (1 mm) + Mo (350 nm) + Al_2O_3 (10 nm)	Drop-Casting in PDDA (1 min)	Drop-Casting 1 h

Table 3.2 - Series of experiments performed on the substrates with a Mo top layer.

Sample	Structure	Functionalization	NPs deposition
MO 1	SLG (1 mm) + Mo (350 nm)	Drop-Casting in PDDA (1 min)	Immersion 1 h
MO 2	SLG (1 mm) + Mo (350 nm)	Drop-Casting in PDDA (1 min)	Drop-Casting 1 h

Table 3.3 - Series of experiments performed on the substrates with a SiO_2 top layer.

Sample	Structure	Functionalization	NPs deposition
SI 1	SLG (1 mm) + Mo (350 nm) + SiO_2 (20 nm)	Drop-Casting in PSS (1 min) + Drop-Casting in PDDA (1 min)	Immersion 24 h
SI 2	SLG (1 mm) + Mo (350 nm) + SiO_2 (20 nm)	Drop-Casting in PSS (1 min) + Drop-Casting in PDDA (1 min)	Immersion 1 h
SI 3	SLG (1 mm) + Mo (350 nm) + SiO_2 (20 nm)	Drop-Casting in PSS (1 min) + Drop-Casting in PDDA (1 min)	Drop-Casting 24 h
SI 4	SLG (1 mm) + Mo (350 nm) + SiO_2 (20 nm)	Drop-Casting in PSS (1 min) + Drop-Casting in PDDA (1 min)	Drop-Casting 1 h

The Au NPs were deposited following the procedures described in the tables above. The samples were characterized with SEM, to verify the aggregates density and size, and were brought to the UV-VIS-NIR spectrophotometer (with the integrating sphere) in order to measure the relative total and diffuse reflection. It is crucial to increase the light's optical path in CIGS ultra-thin solar cells, especially in the range of 700 nm - 1100 nm were an optical thickness higher than 500 nm is needed to absorb all the incident light, as demonstrated in **Section 1.5.** The substrate's diffuse reflection is the parameter that most precisely represents the capability of enhancing the light scattering properties of the substrate. This is because it measures the amount of light that is scattered away from the specular direction, which is related to the amount of photons that have a higher probability to lead to an increase of the EQE by generating photocurrent [39].

The relative total and diffuse reflection measurements of all the produced substrates is shown on **Figure 3.4**. It is important to notice that in all of the reflection plots demonstrated in this work, the abrupt changed verified at 880 nm constitutes an artifact from the measurements and should not been taken in account for their analysis. Besides the samples represented on the tables above, three reference samples with the base structure of each series (represented on each table) were used to study the optical implications of implementing Au aggregates. These reference samples were named REF AL, REF MO and REF SI, and are represented on the plots in **Figure 3.4**.

Figure 3.5 shows the SEM images of the substrates that were determined as the best performing samples, after the Au NP deposition.

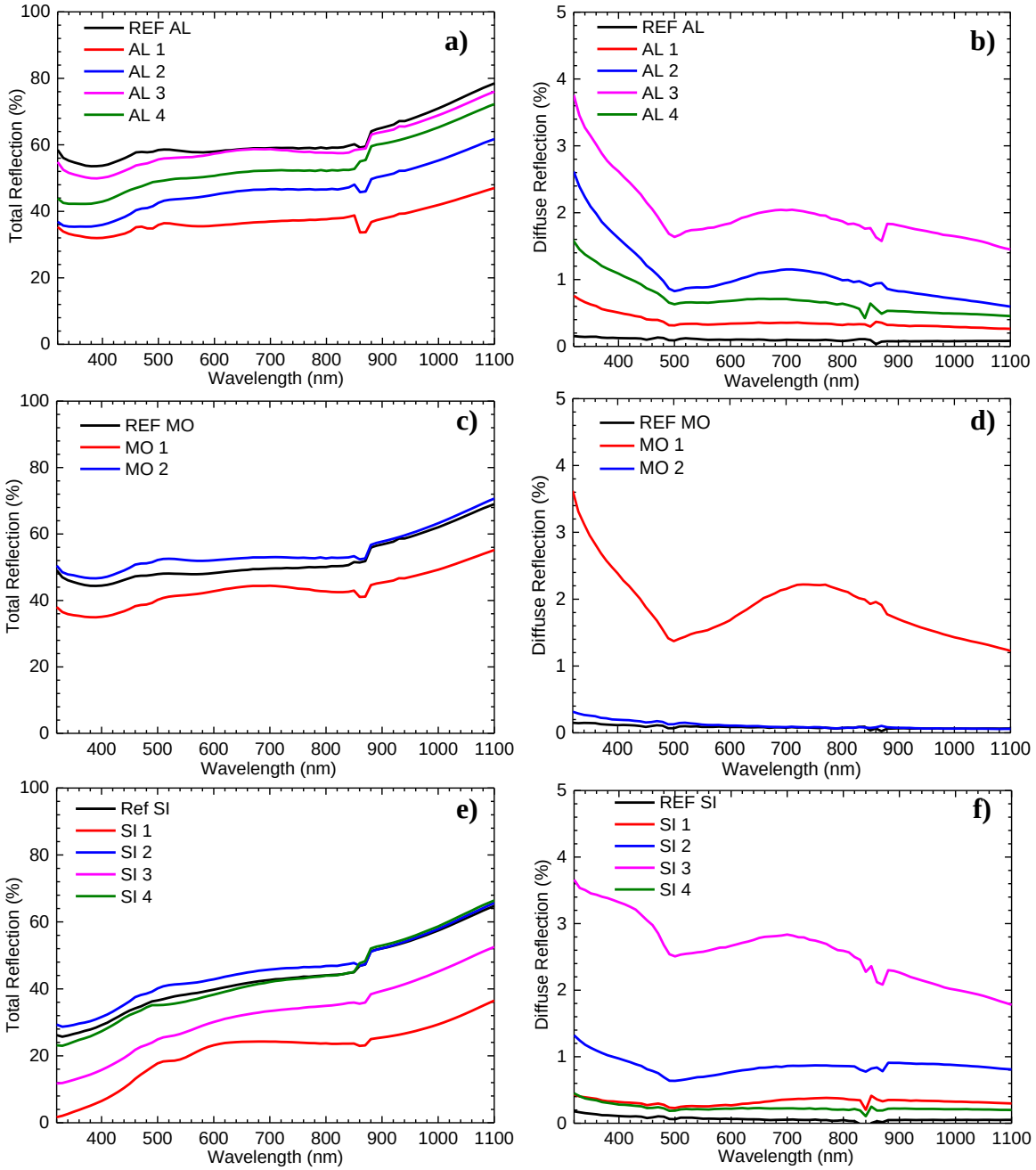

Figure 3.4 - a) Relative total reflection of samples where the deposition was performed on the Al_2O_3 layer; b) Relative diffuse reflection of samples were the deposition was performed on the Al_2O_3 layer; c) Relative total reflection of samples where the deposition was performed on the Mo layer; d) Relative diffuse reflection of samples where the deposition was performed on the Mo layer; e) Relative total reflection of samples where the deposition was performed on the SiO_2 layer; f) Relative diffuse reflection of samples where the deposition was performed on the SiO_2 layer.

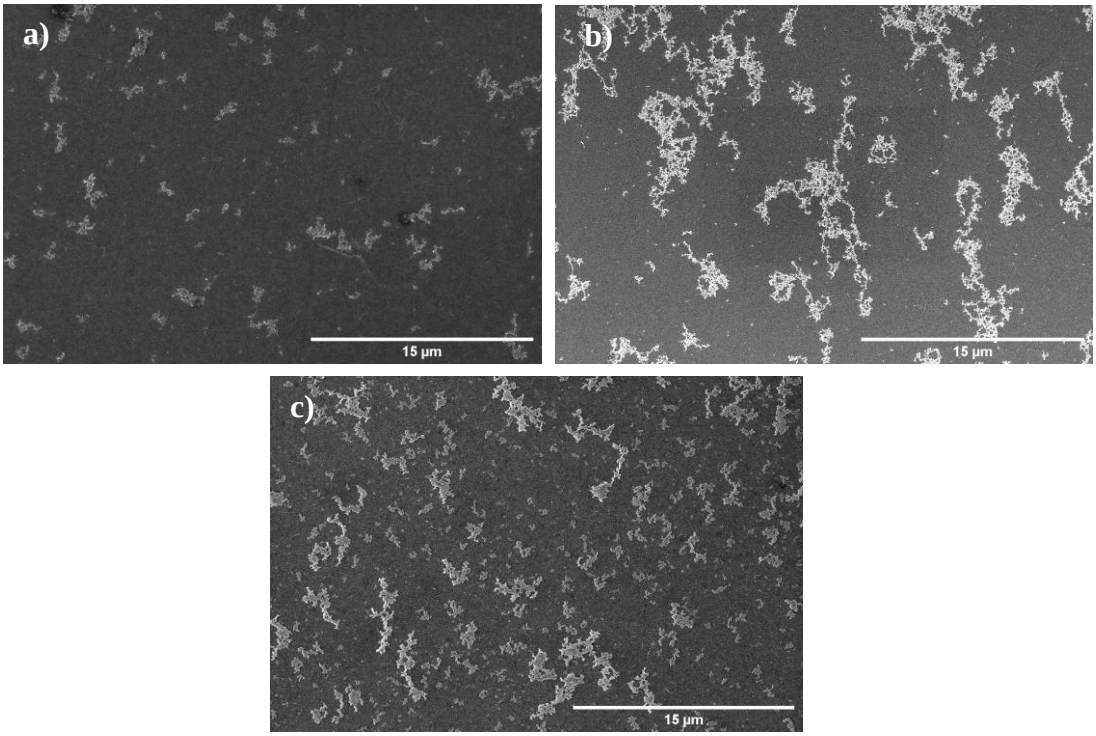

Figure 3.5 - SEM top-view images of the best performing samples with a) the Al_2O_3 layer (AL 2) b) the Mo layer (MO 1) and c) with the SiO_2 layer (SI 3).

From the relative total reflection measurements, when comparing with the reference samples, the samples with added Au NP aggregates, generally, see a decrease in this parameter. Therefore, there are strong indications that these structures will lead to some parasitic absorption. However, there is always an increase in the relative diffuse reflection when the aggregates are added to the substrates. It is also important to consider that the conformal growth of the subsequent layers on top of the Au aggregates may induce some roughness on the subsequent layers. This way, the light optical path will not only be increased through the diffuse reflection from the substrate, but also from the roughness inherent on other layers. It was verified that the increase in the Au NP aggregates in terms of density and size usually leads to higher diffuse reflection. In **Table 3.4**, the surface coverage and the biggest aggregate are represented for each sample. The samples with the higher diffuse reflection, for each corresponding substrate, present the largest aggregates allied with a high surface coverage for each substrate. The exception is sample AL 3 which doesn't have neither the highest surface coverage or the biggest aggregate area and presents the highest diffuse reflection. In this sample, holes are present in the Al_2O_3 layer (**Figure 3.6**), that may have been formed during the deposition process. These aberrations might have led to the high diffuse reflection present in this sample.

Table 3.4 - Average parameters and standard deviation of all samples measured through an SEM analysis.

Sample	Surface Coverage (%)	Biggest Aggregate Area (μm^2)
AL 1	2.41±0.28	1.9
AL 2	3.98±0.56	9.2
AL 3	3.22±1.26	2.2
AL 4	4.57±0.55	1.0
MO 1	4.88±1.23	9.1
MO 2	9.85±1.90	7.5
SI 1	35.52±2.52	0.02
SI 2	6.80±2.49	0.05
SI 3	11.64±0.99	10.3
SI 4	1.65±0.36	2.7

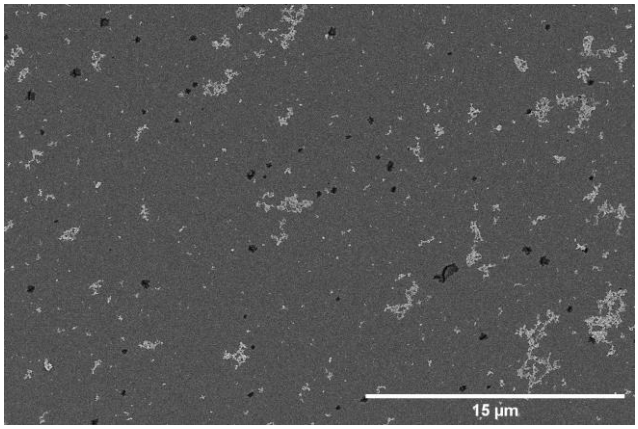

Figure 3.6 - SEM top-view image of sample AL-3.

In terms of relative diffuse reflection, the deposition techniques from the best performing samples were chosen to produce substrates to be implemented in CIGS ultra-thin solar cells. From the series where the substrate's top layers were SiO_2 and Mo, the chosen samples were MO 1 and SI 3 respectively. In the series were the Al_2O_3 top layer was used, the substrate from the sample with the highest diffuse reflection (AL 3) had a lot of cracks that may have led to an increase of the diffuse reflection. Therefore, it was considered that the sample with the second highest diffuse reflection (AL 2), was the more adequate scatterer to be implemented in a solar cell.

For the final device substrate preparation, four 5x5 cm SLG (1 mm) + Mo (350 nm) samples were used for the Au NP deposition. A 10 nm Al_2O_3 layer was deposited in one sample (AL) and a 20 nm SiO_2 layer in another (SI). The deposition methods from the best performing samples were implemented in the respective substrates. In **Table 3.5**, a summary of the developed samples prior to the lithography steps is represented. The relative diffuse reflection of samples AL, MOAL, SI and MOSI is represented on **Figure 3.7.**

Table 3.5 - Summary of the prepared samples with Au aggregates for the final device preparation.

Sample	Structure	NPs deposition method
AL	SLG/Mo/Al_2O_3/Au	Immersion 1h
MOAL	SLG/Mo/Au	Immersion 1h
SI	SLG/Mo/SiO_2/Au	Drop Casting 24 h
MOSI	SLG/Mo/Au	Immersion 1h

From the analysis of the plots on **Figure 3.7** it is clear to see that there are some differences on the relative diffuse reflection when performing the deposition on 5x5 cm substrates. In the case of sample AL we are able to verify an enhancement on the diffuse reflection, however the same cannot be said for the rest of the samples. In order to discuss these variations, the SEM images of each sample are shown in **Figure 3.8** and the parameters extracted from the image's analysis are represented on **Table 3.6**.

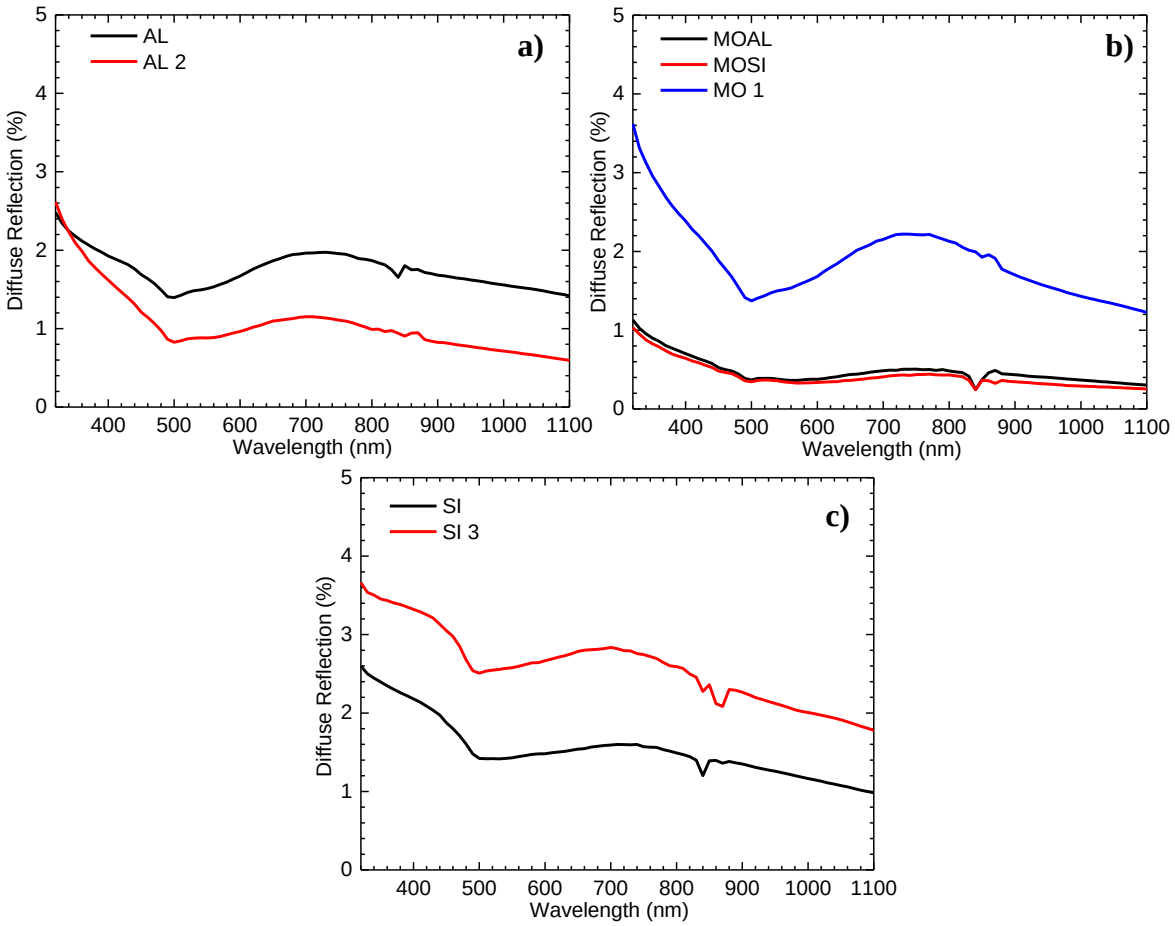

Figure 3.7 - Relative diffuse reflection of a) samples AL and AL2 b) samples MOAL, MOSI and MO 1 c) samples SI and SI 3.

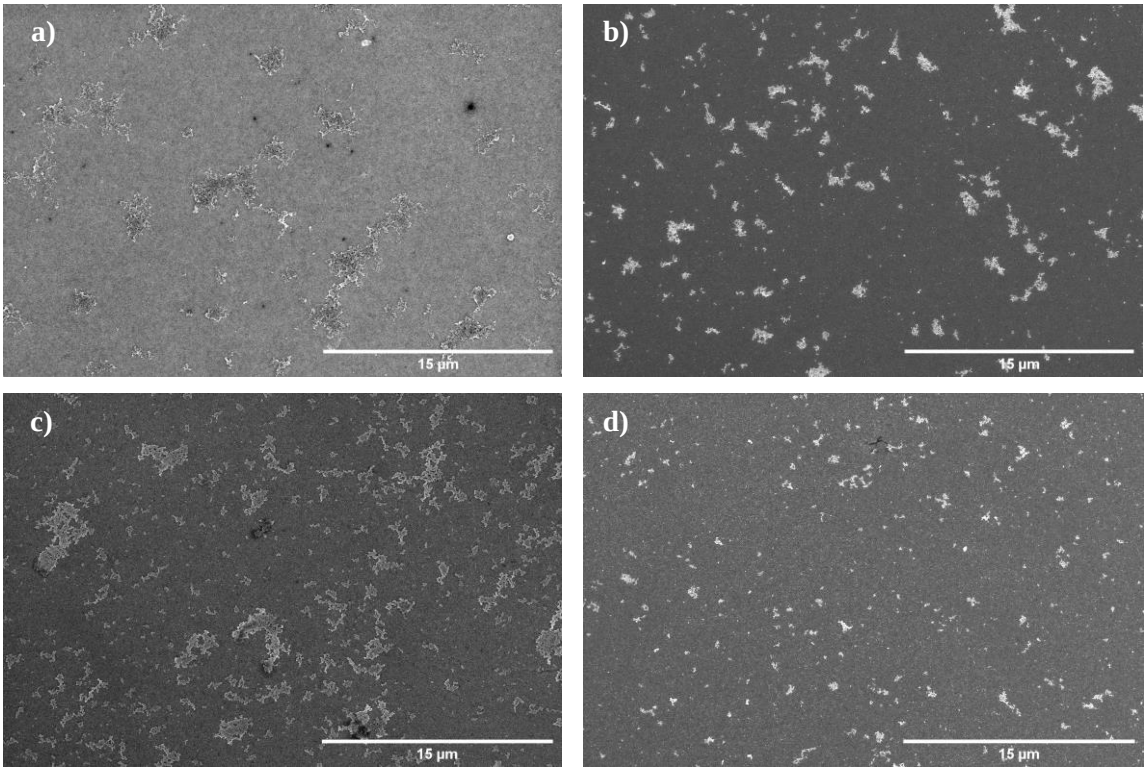

Figure 3.8 - SEM top-view images of a) sample AL, b) sample MOAL, c) sample SI and d) sample MOSI.

Table 3.6 - Average parameters and standard deviations measured through an SEM analysis of samples AL, MOAL, SI and MOSI.

Sample	Surface Coverage (%)	Biggest Aggregate Area (μm^2)
AL	8.2±1.2	7.7
MOAL	4.6±0.7	5.6
SI	9.3±0.2	5.0
MOSI	3.1±0.9	0.5

Sample AL presents a higher surface coverage than sample AL 2, which justifies the enhancement on the relative diffuse reflection. In sample SI, the decrease in the diffuse reflection can be justified by the slight decrease on the obtained surface coverage. However, the changes seen on the previously discussed samples are not as high as the ones visualized on samples MOAL and MOSI, where the area of the obtained aggregates and the surface coverage are clearly inferior than in sample MO 1. Observing the SEM image of sample MO 1 represented before in **Figure 3.5 b)** it is visible that the Au aggregate conformation is very different to the one present on samples MOAL and MOSI. Whereas in sample MO 1 it is possible to see a somewhat web of interconnected aggregates, in sample MOAL and MOSI a predominance of small aggregates with a lower surface coverage is present. Therefore, it can be concluded that the substrate area has an influence on this specific deposition method utilized on the Mo layer. Despite being low, the diffuse reflection is still higher than the reference sample and better than sample MO 2. Therefore, it was decided to proceed with this method for the deposition of Au NPs on Mo layers.

After the aggregate's deposition, the samples were encapsulated with the respective dielectric layers, in order to obtain a 25 nm thick layer in the samples where an Al_2O_3 layer is used (AL and MOAL) and a 30 nm layer in the samples where a SiO_2 layer is used (SI and MOSI). Besides samples AL, MOAL, SI and MOSI, four more samples were prepared for an in-depth study of the influence of the Au NPs aggregates on the solar cell's performance. The mentioned prepared samples are: two reference samples (REF 1 and 2), with no layer deposited on top of the Mo; and two passivated samples, one where the used dielectric layer is Al_2O_3 (ALPASS) and another where the dielectric layer is SiO_2 (SIPASS). In **Table 3.7**, a summary of the samples prepared for the final devices fabrication is represented.

Table 3.7 - Summary of all the prepared substrates for the final device fabrication.

Sample	Structure
REF 1	SLG (1 mm) /Mo (350 nm)
REF 2	SLG (1 mm) /Mo (350 nm)
ALPASS	SLG (1 mm) /Mo (350 nm) /Al_2O_3 (25 nm)
SIPASS	SLG (1 mm) /Mo (350 nm) / SiO_2 (30 nm)
AL	SLG (1 mm)/Mo (350 nm)/Al_2O_3 (10 nm)/Au aggregates/Al_2O_3 (15 nm)
MOAL	SLG (1 mm)/Mo (350 nm)/Au aggregates/Al_2O_3 (25 nm)
SI	SLG (1 mm)/Mo (350 nm)/SiO_2 (20 nm)/Au aggregates /SiO_2 (10 nm)
MOSI	SLG (1 mm)/Mo (350 nm)/ Au aggregates /SiO_2 (30 nm)

In **Figure 3.9**, the relative diffuse reflection of samples AL, MOAL, SI and MOSI after the deposition of the dielectric layers is represented. When the Au NP aggregates are encapsulated through the deposition of the dielectric layer, there is a slight decrease of the relative diffuse reflection. This effect is expected if a conformal deposition of the dielectric layer is assumed. This way, the substrate after the encapsulation has a more planar top surface, which causes the decrease seen in the diffuse reflection. In the case of the samples where a SiO_2 layer was used, another effect can be responsible for the observed decrease. The mentioned effect is the melt of the Au NPs due to the high temperatures (300 ºC) used during the PECVD deposition of the SiO2 layer. SEM images (**Figure 3.10**) taken on sample SI show that after the encapsulation process the Au NPs and the aggregates become flatter, therefore the roughness inherent to the aggregates will decrease.

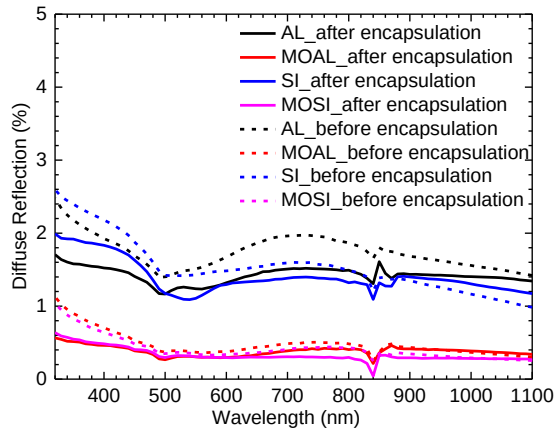

Figure 3.9 - Relative diffuse reflection of the prepared substrates before (solid lines) and after (dashed lines) encapsulation.

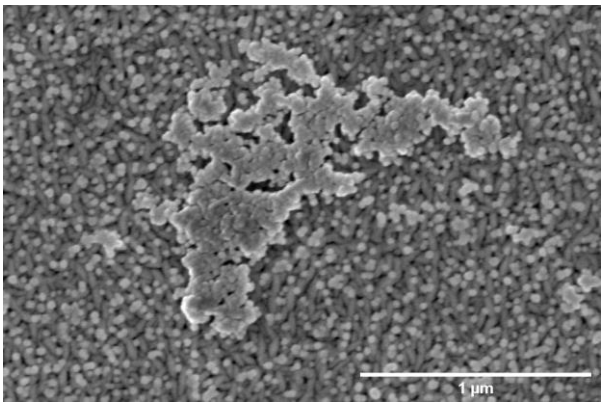

Figure 3.10 - SEM top view image of sample SI after encapsulation.

As the final step for the substrate preparation, all but the reference samples were submitted to a lithographic process to produce line contacts in the dielectric layer, in order to have an ohmic contact between the CIGS layer and the Mo layer. The plots of the relative total and diffuse reflection after the lithographic procedure are represented on **Figure 3.11**. As it was discussed before, the introduction of Au aggregates leads to a reduction of the relative total reflection. However, the final substrates demonstrate again a higher diffuse reflection for the samples with Au aggregates compared with the passivated and reference samples. Despite the decrease in the total reflection, a higher diffuse reflection shows the possibility of increasing the solar cell J_{sc} in ultra-thin solar cells through the increase of the light's optical path inside the CIGS layer, since a high specular reflection leads to light directly leaving the solar cell.

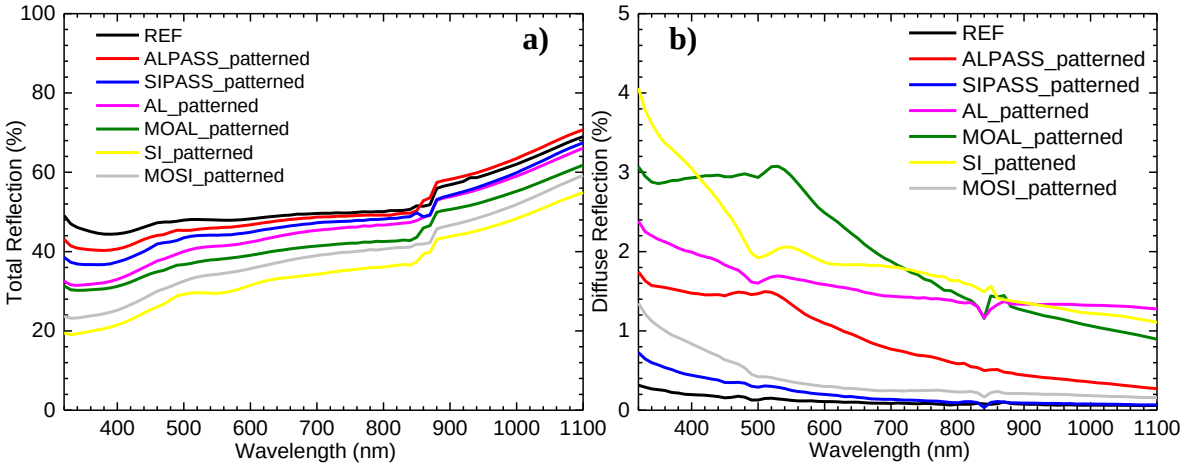

Figure 3.11 - a) Relative total reflection of all substrates after patterning; b) Relative diffuse reflection of all substrates after patterning.

AFM images (**Figure 3.12 a)**) of all samples were taken, allowing for the determination of various parameters that can be of critical understanding for the solar cell's performance. These are represented on **Table 3.8**. Through the analysis of the AFM images, the pitch and feature size of the produced structures were measured. The obtainable feature size is bigger than the expected (700 nm). Hence, the passivation area is reduced and a detriment on the ability to reduce the rear surface recombination can occur [61]. However, this is not critical for the main purpose of this work, since the goal is to understand the effects of the introduction of aggregates on the solar cell's performance. Furthermore, the main role of the Al_2O_3 layer here is to serve as an encapsulation layer to the Au aggregates. Another problem that was verified with the AFM analysis and further confirmed with a SEM analysis (**Figure 3.12 b)**) was the incomplete etch of the Au NPs inside the trenches. The Au present in

the trenches is, therefore, free to diffuse into the CIGS layer, due to the high temperatures (~500 ºC) achieved during the absorber growth. As shown in [20], the diffusion of metals into the CIGS layer can have degradational effects in the electrical performance of the final device. It is also important to consider the high average aggregate height in each sample, since the pyramidal conformation of the Au aggregates can create problems during the CIGS growth, leading to degradational effects to the solar cell's performance.

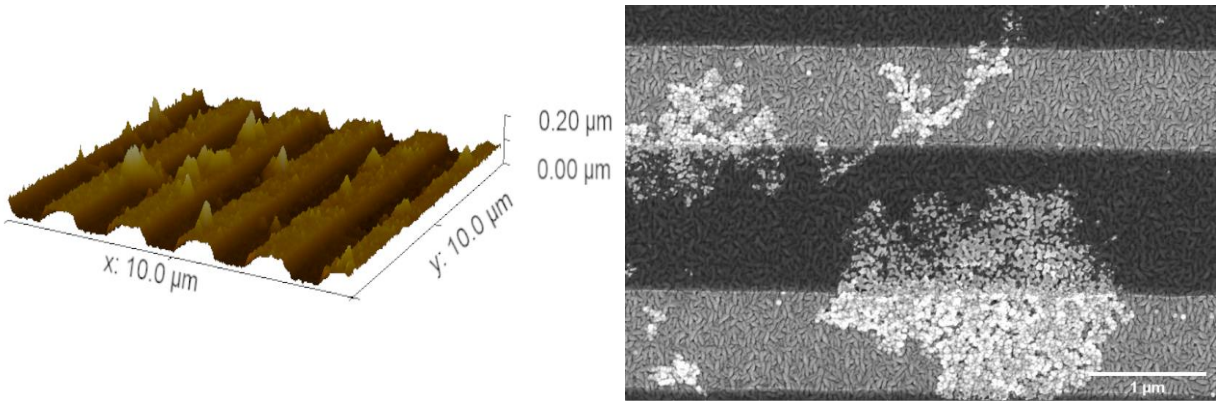

Figure 3.12 - AFM image (left) and SEM top view image (right) of sample MOAL

Table 3.8 - Average parameters and standard deviation measured through an AFM analysis of the patterned samples.

Sample	Line width (nm)	Pitch (µm)	Average aggregate height (nm)
ALPASS	928±16	2.05±0.02	N/A
SIPASS	928±20	2.03±0.02	N/A
AL	914±73	2.06±0.02	139.66±29.74
MOAL	882±37	2.06±0.02	95.12±20.60
SI	922±20	2.00±0.02	135.00±31.06
MOSI	770±38	2.04±0.03	85.90±29.95

3.3.2 Optical simulations

A substrate with Au aggregates was brought to the AFM and the measured data was utilized to represent the Au aggregates on the optical simulations of the complete solar cell stacks. An area with a high density of aggregates was chosen so that the simulations are performed in the optimized optical conditions. The Au aggregates roughness was also translated to the subsequent top layers, assuming a conformal growth of the deposited layers on top of them. All the prepared substrate structures were studied in this section, so for simplicity, the simulation names will correspond to the sample's names. For clarification reasons, the simulation setup of sample MOAL is represented on **Figure 3.13**.

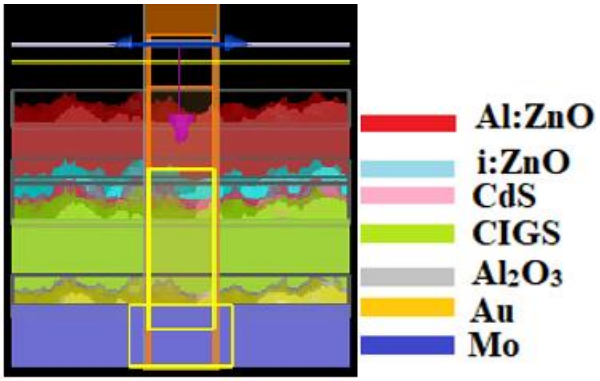

Figure 3.13 - MOAL simulation setup.

The simulations performed in this section were based in the same numerical model as the ones on **Section 3.1.1**. However, the accuracy tests could not be performed on the structures with Au aggregates. This is because the analytical results cannot account for the influence of the roughness on the solar cell absorption. However, the validation obtained from the simulations in **Section 3.1** indicate that the validity of the simulations performed in this section should be trustful. The calculated absorption in the CIGS and substrate layers are represented on **Figures 3.14 a)** and **c)**, the solar cell's total reflection is represented on **Figures 3.14 b)** and **d)**, and the calculated J_{sc} are represented on **Table 3.9**.

Before going into the analysis of the Au aggregates in the solar cell's optical behavior, it is important to study the optical effects of the different encapsulation/passivation layers. Through the addition of the dielectric layers a ~0,5 mA/cm^2 J_{sc} enhancement is verified in comparison to the reference sample. The decrease in the substrate parasitic absorption indicates that the verified enhancement might be a result of an increase in the rear optical reflection. Therefore, the introduction of the dielectric layers leads to the mitigation of some of the optical losses that occur in ultra-thin solar cells. This effect has already been demonstrated in previous works [20], [31], [62].

With the introduction of Au NP aggregates, a broadband enhancement of the light absorbed in the CIGS layer is verified, resulting in a ~1.6 mA/cm^2 J_{sc} increase with respect to the passivated layers. For wavelength values lower than 750 nm the roughness induced by the Au NP aggregates leads to a decrease in the light reflected from the top surface of the solar cell, as it is shown in **Figures 3.14 b)** and **d)**. The improvement in the anti-reflection behavior in the solar cell top layers is, therefore, the main responsible for the verified enhancement in this wavelength range. The reflection decrease due to the front surface texturing is something that has been explored successfully in previous works [63], [64]. The decrease verified in the substrate parasitic absorption, for wavelength values higher than 750 nm, indicates that the increase verified in this range resulted mostly from the enhanced rear scattered light. The increase in the light scattered in the top surface must also be considered since it may also contribute to an enhancement on the light's optical path inside the CIGS layer. However, as demonstrated in previous studies [63], [64], this increase also leads to an enhanced parasitic absorption in the solar cell's top layers.

It is important to consider that the performed simulations only take into account the optical effects of the introduction of Au NP aggregates in the solar cell stack and do not consider the detrimental effects that the Au NP aggregates can have on the solar cell's electrical performance that will be further explored in the next section.

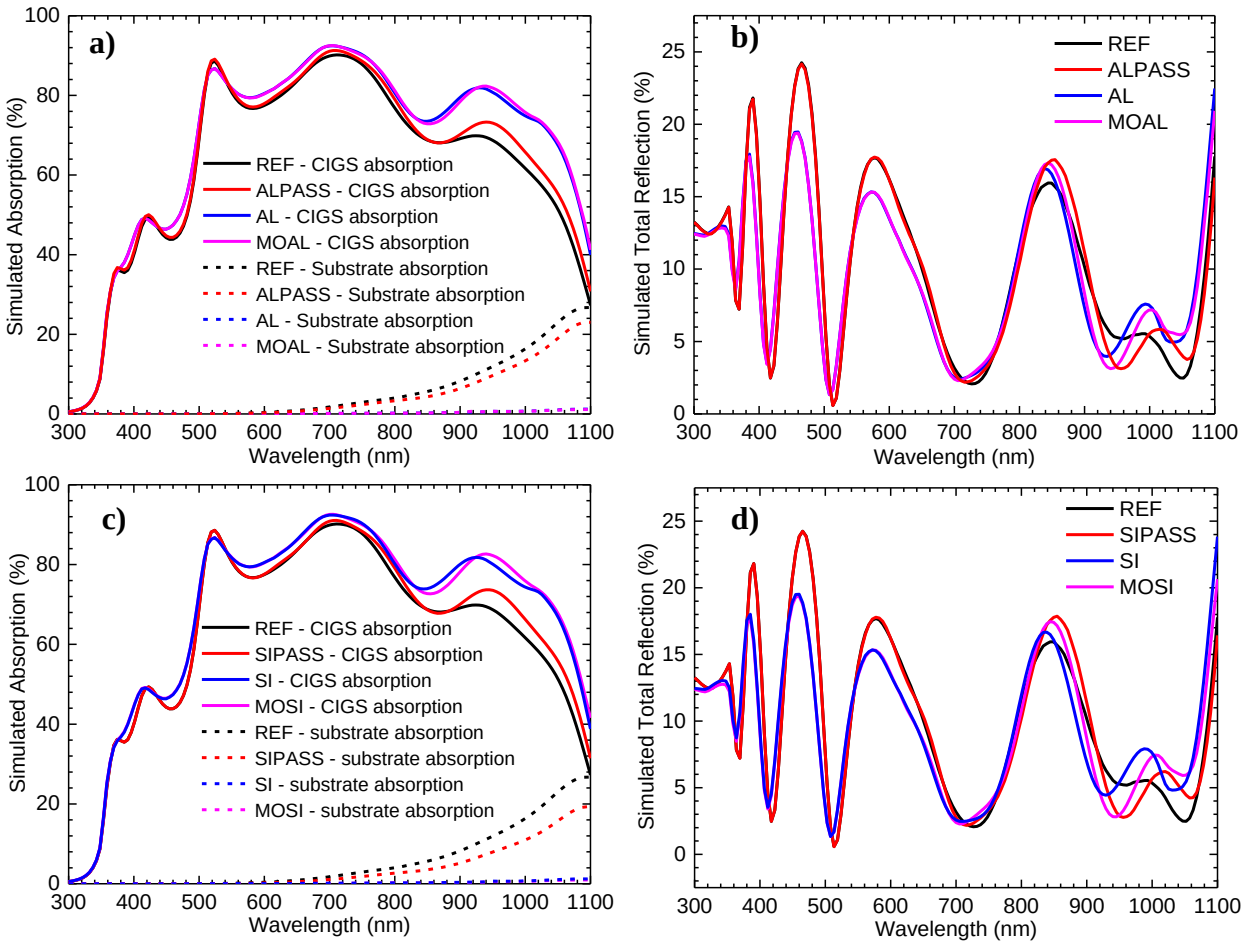

Figure 3.14 - a) Simulated absorption in the CIGS (solid lines) and substrate (dashed lines) of samples REF, ALPASS, AL, and MOAL; b) Simulated total reflection of samples REF, ALPASS, AL and MOAL; c) Simulated absorption in the CIGS (solid lines) and substrate (dashed lines) of samples REF, SIPASS, SI and MOSI; d) Simulated total reflection of samples REF, SIPASS, SI and MOSI.

Table 3.9 - Simulated J_{sc} from all samples.

Sample	J_{sc} (mA/cm^2)
REF	27.41
ALPASS	27.99
SIPASS	27.94
AL	29.60
MOAL	29.62
SI	29.56
MOSI	29.62

3.3.3 Optoelectronic characterization

During the transportation to imec, sample AL broke and it wasn't possible to fabricate the solar cell set in this sample. However, the devices were fabricated in the remaining 7 samples. 32 solar cells with a 0.5 cm^2 area were produced in each sample. Before the analysis of the complete devices it is important to consider that the CIGS deposition in each sample wasn't performed at the same time. This was due to limitations on the co-evaporation equipment in imec, where only two samples could be utilized per run. **Table 3.10** summarizes the CIGS characteristics for each run, along with the samples that were submitted to each run.

Table 3.10 - Summary of the as-deposited CIGS characteristics for the different CIGS deposition runs.

CIGS Run	Samples	CGI	GGI	Thickness (nm)
1	REF 2 + MOAL	0.8	0.3	462
2	ALPASS+ REF 1	0.81	0.29	475
3	SI + SIPASS	0.75	0.31	436
4	MOSI	0.78	0.31	442

The J-V illuminated and dark curves of every sample are represented on **Figures 3.15 a)** and **b)** and the parameters extracted from the J-V and EQE analysis are summarized on **Table 3.11**. The solar cell's advanced parameters are represented on **Table 6.2** in **Annex 3**. The solar cell's figures of merit were extracted from the J-V measurements, except the J_{sc} that was calculated from the EQE curves through the following equation:

$$J_{sc} = q\int \frac{\lambda}{hc} EQE(\lambda) I_{AM\,1.5}(\lambda)\, d\lambda \tag{3.8}$$

The reference samples that were sent to imec with only a Mo layer deposited on top of the SLG present efficiency values drastically different. REF 1 has an efficiency value of 6.8 % while REF 2 has an efficiency value of 5.5 %. This electrical performance difference is due to the complex CIGS properties that changes from run to run. The CGI and GGI ratios present fairly close values in between runs. The V_{oc} values are similar, the difference in the efficiency stems mostly from a decrease in the J_{sc}. So, the performance discrepancy from both reference samples could stem from the difference between the CIGS thickness. The *FF* of REF 2 is also considerably lower than REF 1. Typically, the reduction of a CIGS solar cell thickness leads to a decrease in the light's optical path therefore decreasing J_{sc}. This way more light is also absorbed in the Mo rear contact that otherwise would be collected. The thinner the absorber layer, the higher is the risk of shunts which would cause an increase on the *FF* [65]. Although the obtained results are in concordance with what is expected with a decrease of the absorber layer thickness, a 13 nm thickness variation shouldn't cause the observed inconsistency between both samples. Therefore, the disparity seen between the references is most likely related to factors associated with the CIGS co-evaporation deposition, such as, the temperature profile along the deposition process, the metal source control, amongst others. In [27], where Lindahl *et al.* optimized the in-line co-evaporation CIGS deposition process, an 2 % (abs) efficiency variation amongst samples from different runs was obtained. Therefore, the 1.3 % (abs) variation seen between the references is not inconceivable. Despite that, the obtained results demonstrate that in order to perform accurate comparisons between samples, these should belong to the same deposition run.

According to previous results [31], the passivation capabilities of the Al_2O_3 layer, discussed in **Section 1.4**, induce an improvement in the device performance. An increase of the solar cell's V_{oc}, due to the decrease of the defect concentration on the interface is expected alongside with an increase in $J_{sc,}$ derived from the combination of electrical and optical effects [31]. However, when samples REF 1 and ALPASS are compared, the efficiency slightly drops with the introduction of the dielectric layer. This result stems from two factors: the solar cell passivated area (discussed in **Section 3.3.1)** and deposition process were not optimized to attain a high passivation performance during this work. When sample SIPASS (passivated SiO_2 sample) is compared with both references, the efficiency of this sample is scarcely higher than in sample REF 2 and is worse than sample REF 1. However, the absorber in this passivation layer is largely thinner than in both references, as it can be seen on **Table 3.10**. Therefore, it may be possible that the addition of SiO_2 may have led to beneficial effects. However, with the

obtained results a reasonable assessment is not possible to be made. Despite the poor performance of the passivation layers, the main goal of this work was to use them mostly as the encapsulation layer of the Au NP aggregates.

The implementation of Au NP aggregates seems to have detrimental effects in the device's V_{oc} and *FF*, as it is shown by the lower values of these parameters in samples MOAL, SI and MOSI with respect to the corresponding passivated and reference samples. With the introduction of the Au aggregates there is an increase of the ideality factor (*A)* (**Table 6.2** in **Annex 3**) to values above 1.8 in all of the considered samples. According to [66], this increase might have resulted from an increase of the interface recombination rate and/or an increase in the space-charge region (SCR) recombination rate. The inherent roughness of the Au NP aggregates may have led to an increase of the rear interface defect density, which would increase the rear interface recombination. The increase of the SCR recombination rate might have resulted from the diffusion of the Au, from the NPs present in the line contacts after the etching procedure (**Section 3.3.1**), into the CIGS layer. With the addition of the Au aggregates, there is also a decrease in R_p. The roughness inherent to the Au aggregates may facilitate the formation of pinholes in the CIGS layer, which can shorten the p-n junction, explaining the decrease in R_p. At last, the R_s also increases with the employment of the aggregates. The main R_s limitation comes from the transparent conductive oxides (TCOs) i:ZnO and Al:ZnO sheet resistance [67]. With the introduction of Au aggregates and the expected conformal growth of all the layers, the aggregates roughness will also be translated to the TCO layers. The top surface texturization might increase the charge carrier's path until they can be collected by the metallic grid, increasing the R_s. The variations verified in the solar cell's *A*, R_p and R_s can justify the observed variations in the V_{oc} and *FF*, and consequently, the drop in their efficiency values as compared to the reference and passivated samples.

Despite the lower performance of the samples with Au aggregates, compared with the references, the most important parameter in this analysis would be the J_{sc}, since it would allow to prove the optical enhancement verified by the performed optical simulations in **Section 3.3.2**. In samples SI and MOSI, where the passivation layer is SiO_2, there is an unexpected decrease of the J_{sc} when comparing with sample SIPASS, which may be related to the very high R_S values of these substrates. The 20 second reactive ion etching procedure utilized for these samples might not have been enough to completely etch all the SiO_2 layer below the Au NP aggregates. This might explain why these two samples present the highest R_s values amongst all samples. However, in sample MOAL an increase of 3.3 mA/cm^2 in the J_{sc} is verified when compared with the reference submitted to the same run. When comparing the EQE curves of samples MOAL and REF 2 (**Figure 3.16 a)**), it is possible to verify a broadband enhancement, as obtained by the performed simulations on **Section 3.3.2**. The relative total reflection of sample MOAL and REF 2 are represented on **Figure 3.16 b)**. At lower wavelength values, the lower optical reflection verified in sample MOAL points out to the improvement of the anti-reflective properties with the introduction of the Au aggregates. The verified enhancement might have resulted from the roughness induced from the conformal growth over the Au NP aggregates of the subsequent layers. The reduced reflection is, therefore, the main responsible for the EQE enhancement for wavelength values lower than 750 nm, especially because in this wavelength range most of the light is absorbed in the CIGS layer without interacting with the Au aggregates. At longer wavelength values, besides the influence of the anti-reflection improvement, the observed EQE increase might have also been a result of the longer light optical path in the CIGS layer, produced by the increased scattering at the solar cell rear contact. Similar results were obtained by Morawiec *et al.* [39], where the utilization of plasmonic Ag NPs also led to a broadband EQE enhancement of a n-i-p- a-Si:H solar cell. In this work the authors concluded that the enhancement in the IR range was due to the plasmonic scattering of the NPs implemented in the rear substrate. Whereas, the enhancement in the visible region of the spectrum resulted from the roughness created at the front surface that can act as an anti-reflective coating.

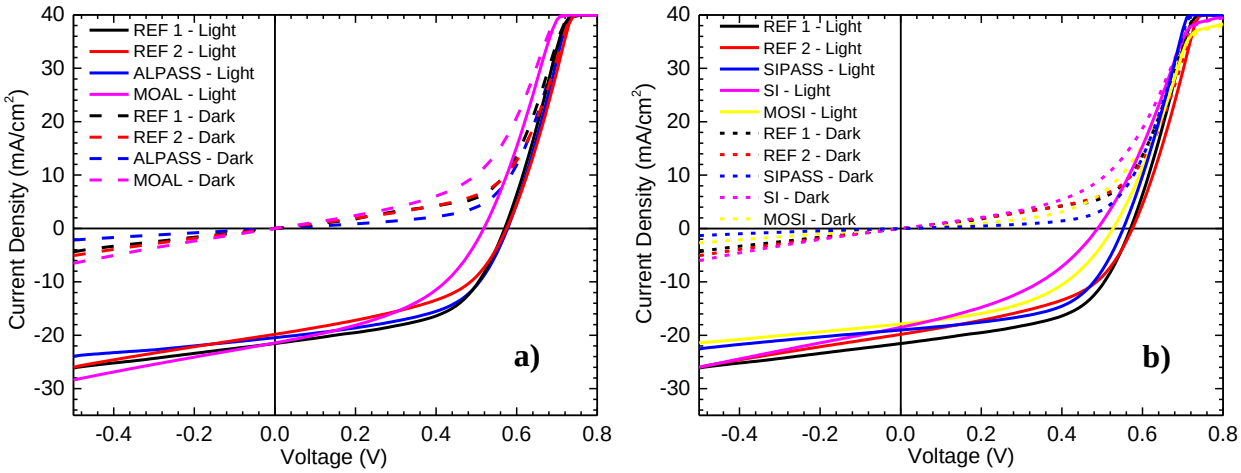

Figure 3.15 - Illuminated (solid lines) and dark (dashed lines) J-V characteristics of a) samples REF 1, REF 2, ALPASS and MOAL and b) samples REF 1, REF 2, SIPASS, SI and MOSI.

Table 3.11 - Averages and standard deviations of the final devices figures of merit.

Sample	**Structure**	***V_{oc}* (mV)**	***J_{sc}* (mA/cm^2)**	***FF (%)***	***eff (%)***
REF1	Mo	566±31	20.62±1.79	54.36±11.62	6.77±1.78
REF2	Mo	572±27	18.11±1.96	48.88±8.14	5.54±1.14
ALPASS	Mo/Al_2O_3	571±61	19.24±0.77	55.99±8.14	6.65±0.39
SIPASS	Mo/SiO_2	552±6	18.75±0.47	55.84±4.30	5.89±0.59
MOAL	Mo/Au/Al_2O_3	516±25	21.39±2.09	44.12±6.15	4.94±1.06
SI	Mo/SiO_2/Au/SiO_2	487±40	16.97±0.83	39.93±4.91	3.66±0.95
MOSI	Mo/Au/SiO_2	526±23	17.05±0.62	47.32±6.77	4.60±0.97

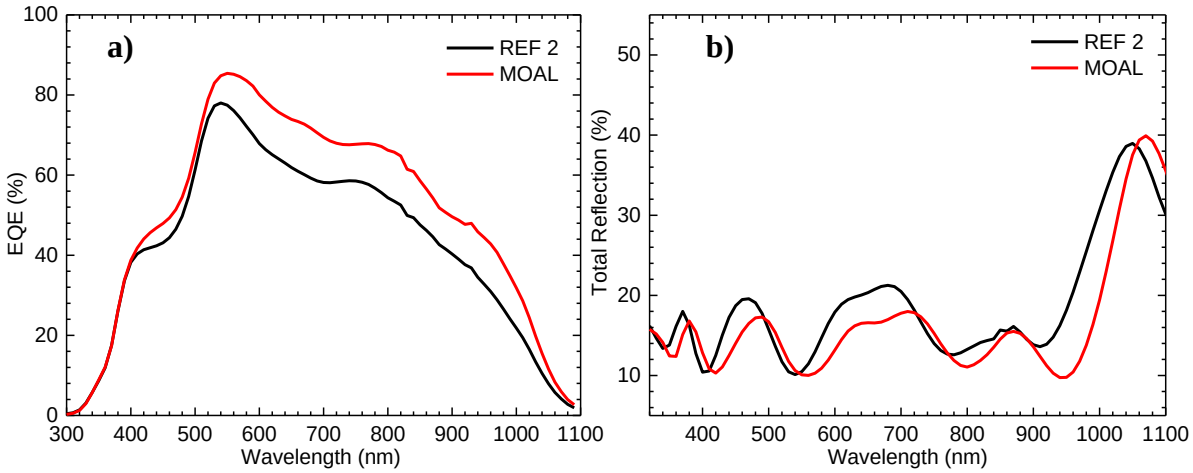

Figure 3.16 - a) EQE curves and b) Relative Total Reflection of samples REF 2 and MOAL.

3.4 Optimization of the NPs monolayer deposition

The deposition process used in this section was based on the work performed by Alexandra Teixeira *et al.* [42]. However, in the process developed in this thesis, the substrate is functionalized with an amino-silane (APTMS). The deposition process was performed with the intent of forming a self-assemble monolayer (SAM) of APTMS. The deposited silane has positively charged end-groups that can attract negatively charged compounds [38]. As referred before, the synthetized Au NPs have a negatively charged end group provided by the stabilizing agent in the colloidal solution. Therefore, the NPs are able to electrostatically bond to the deposited SAM and repel other NPs that can be deposited in that spot [38]. After the substrate functionalization a reservoir-like PDMS structure was used, as described in **Section 2.1.2**. The use of this PDMS structures allows for a control of the evaporation of the NP colloidal solution solvent to achieve a homogeneous deposition of the NPs [42]. The combined action of the SAM monolayer, produced by the silanization process, with the controlled deposition, achieved using the PDMS reservoir, is expected to avoid the formation of NP aggregates during the Au NP deposition.

As discussed before, NPs with a 59.12 nm radius were synthesized to develop this procedure. Three different concentrations of the Au NP solution were used (0.25 mM, 0.5 mM and 1 mM). The Au NP deposition was only tested on an Al_2O_3 top layer, and all the depositions were performed on the same substrate. The SEM images of the deposited NPs for the different concentrations are represented on **Figures 3.17 a)**, **b)** and **c)**. The utilized process enabled the deposition of individual NPs with a minimal presence of aggregates for every used concentration. As it can be seen by the results presented on **Table 3.12**, as the NP solution concentration is increased, the surface coverage of the Au NPs also increases. The surface coverage values are still low. However, this process is still in optimization phase and further developments can be made to increase the surface coverage of the deposited NPs, such as, further increase of the Au NP solution concentration, a variation of the sodium citrate concentration on the Au NP solution or even an increase of the NP deposition time until the complete evaporation of the solvent is verified. The study of the substrate's reflection was also not possible, since the deposition area of the Au NPs is limited by the size of the PDMS reservoir, which was not optimized for the performed study. For further studies, it is crucial to produce master molds that will allow the fabrication of PDMS devices with bigger areas, therefore allowing the deposition of Au NPs in bigger areas, in which their contribution in the substrate total and diffuse reflection can be studied.

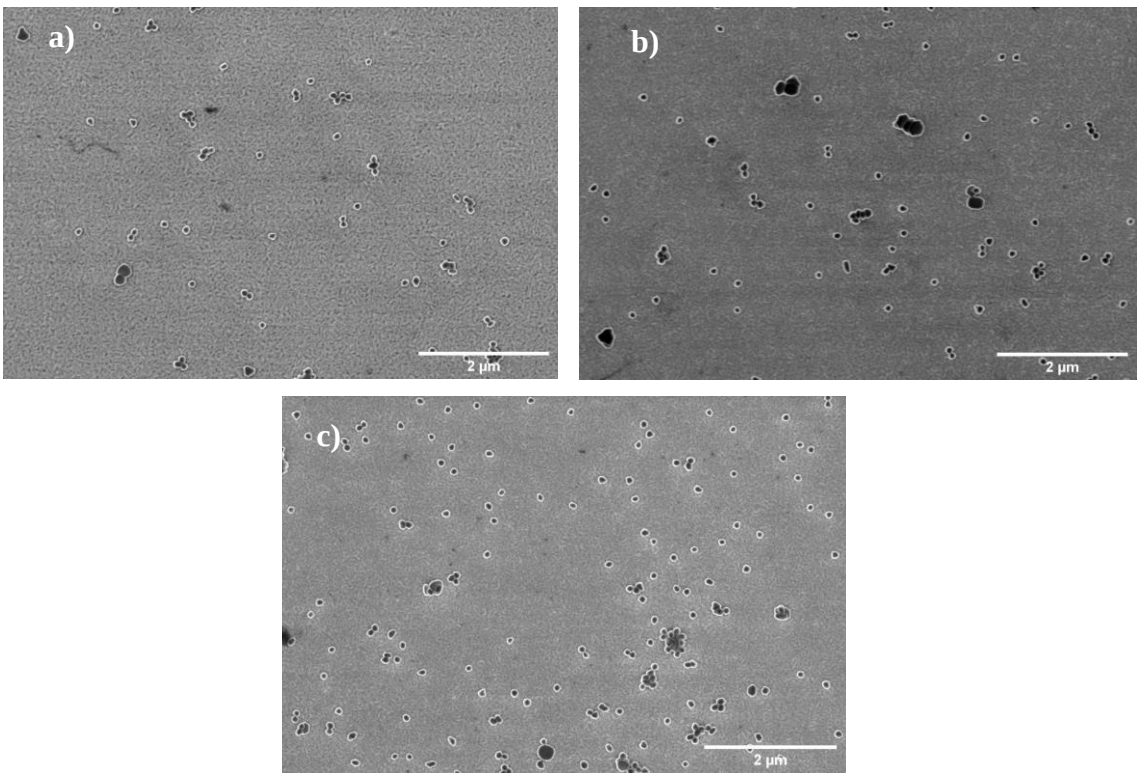

Figure 3.17 - SEM images of deposited NPs on an Al2O3 substrate with a concentration of a) 0.25 mM, b) 0.5 mM and c) 1 mM.

Table 3.12 - Average surface coverage and standard deviation obtained through SEM analysis.

Concentration (mM)	Surface Coverage (%)
0.25	1.63±0.11
0.5	2.04±0.39
1	4.47±1.11

4 Conclusions and future perspectives

The main objective of this work was the development of light management approaches in CIGS solar cells through the utilization of Au NPs. The NPs were implemented through two different approaches at the solar cell's rear contact with the intent of improving the device's light trapping capabilities.

The first approach consisted on the implementation of Au NP aggregates at the rear contact of CIGS solar cells. The deposition of Au aggregates was optimized for different layers, and through UV-VIS-NIR spectrophotometry measurements, a diffuse reflection enhancement of the samples with Au aggregates was verified with comparison to reference samples, demonstrating the possibility of increasing the light's optical path inside the CIGS layer with the implementation of this structures. For the preparation of the rear solar cell contacts a line contact pattern with a line width of 700 µm and a 2 µm pitch was desired. However, the obtained patterned demonstrated a line width with 900 µm, that can potentially degrade the beneficial effects obtained with the introduction of the passivation layer. The reactive ion etching process was also ineffective to completely etch all the Au NPs inside the line contacts, which could possible allow the Au diffusion into the CIGS layer, due to the high temperatures achieved (~500 ºC) during the absorber growth. Optical simulations, conducted through the commercial Lumerical software with the fabricated rear contacts, demonstrated the benefits that the integration of Au aggregates at the rear contact can have in terms of their light trapping capabilities. The simulated device structures demonstrated a 1.6 mA/cm^2 J_{sc} improvement relative to the passivated cells and a 2.1 mA/cm^2 improvement relative to the reference. Such increase was attributed to the increased rear scattering and an improvement of the anti-reflection properties stemming from the texturization of the top layers caused by the Au aggregates. The improvements obtained in the simulation medium were practically demonstrated in sample MOAL, as a broadband EQE enhancement, that translated on to a 3.3 mA/cm^2 J_{sc} increase (relative to the reference sample) was demonstrated. The positive results obtained with the implementation of this architecture were, however, insufficient to obtain an improvement on the solar cell's efficiency values. All of the developed solar cells with Au aggregates demonstrated lower efficiency values than their passivated and reference counterparts, stemming mostly from a V_{oc} and FF values drop. The decrease in the referred figures of merit was attributed mainly to the Au diffusion into the absorber layer, and to the increase in the rear interface defect density. The poor efficiency values demonstrate that this process is still far from optimized. Further improvements in the development process of the rear contact are required for the viable integration of this approach in CIGS solar cells, such as: an improvement on the etching process is required in order to efficiently etch all of the Au material in the line contacts; and an optimization of the optical lithography process is needed to fully exploit the positive effects that the passivation layer can demonstrate.

In the second approach, the deposition of individual NPs with a minimal presence of aggregates was achieved through the use of a PDMS "reservoir-like" architecture and the silanization process combined action. However, the obtained surface coverage is still far from the desired monolayer, indicating the necessity of refining the Au NPs deposition process. Various deposition parameters that can be optimized were identified and are as follows: the Au NP solution concentration, the sodium citrate concentration on the Au NP solution and the NP deposition time. Furthermore, the utilized PDMS structures were not developed for the present study. Therefore, for a clear visualization of the benefit effects of implementing high scattering Au NPs in CIGS solar cells, a new PDMS reservoir is needed so that a bigger NP areas can be produced, enabling other optical measurements.

5 References

[1] M. Schmid, "Review on light management by nanostructures in chalcopyrite solar cells," *Semiconductor Science and Technology*, vol. 32, no. 4. Institute of Physics Publishing, Mar. 2017.

[2] P. Cunha, "Deposition and characterization of CdS and ZnO:Al thin films for Cu(In,Ga)Se 2 solar cells." Master's Thesis, Universidade do Minho, Oct. 2016.

[3] B. Brady, P. H. Wang, V. Steenhoff, and A. G. Brolo, "Nanostructuring Solar Cells Using Metallic Nanoparticles," in *Metal Nanostructures for Photonics*, Elsevier Ltd., pp. 197–221, 2019.

[4] G. Yin, P. Manley, and M. Schmid, "Light trapping in ultrathin $CuIn_{1-x}Ga_xSe_2$ solar cells by dielectric nanoparticles," *Sol. Energy*, vol. 163, pp. 443–452, Mar. 2018.

[5] "2019." [Online]. Available: http://www.solar-frontier.com/eng/news/2019/0117_press.html. [Accessed: 17-Sep-2019].

[6] O. Donzel-Gargand, "The Multiple Faces of Interfaces: Electron microscopy analysis of $CuInSe_2$ thin-film solar cells" Doctoral Dissertation, Uppsala Universitet, 2018.

[7] J. Ramanujam and U. P. Singh, "Copper indium gallium selenide based solar cells - A review," *Energy and Environmental Science*, vol. 10, no. 6. Royal Society of Chemistry, pp. 1306–1319, Jun. 2017.

[8] W. Ananda, "External quantum efficiency measurement of solar cell," in *QiR 2017 - 2017 15th International Conference on Quality in Research (QiR): International Symposium on Electrical and Computer Engineering*, pp. 450–456, Dec. 2017.

[9] P.M.P. Salomé, "Chalcogenide Thin Films for Solar Cells: Growth and Properties," Doctoral Dissertation, Universidade de Aveiro, 2011.

[10] F. Meillaud, A. Shah, C. Droz, E. Vallat-Sauvain, and C. Miazza, "Efficiency limits for single-junction and tandem solar cells," *Sol. Energy Mater. Sol. Cells*, vol. 90, no. 18–19, pp. 2952–2959, Nov. 2006.

[11] "PV Performance Modeling Collaborative | Single Diode Equivalent Circuit Models." [Online]. Available: https://pvpmc.sandia.gov/modeling-steps/2-dc-module-iv/diode-equivalent-circuit-models/. [Accessed: 17-Sep-2019].

[12] S. M. Sze . Kwok K. Ng, *Physics of Semiconducting Devices*, Third. United States of America: John Wiley & Sons, Inc., Hoboken, New Jersey, 2007.

[13] Lepetit Thomas, "Influence of KF post deposition treatment on the polycrystalline Cu(In,Ga)Se_2/CdS hetero-junction formation for photovoltaic application," Doctoral Dissertation, Univ. Nantes, Nov. 2015.

[14] K. L. Chopra, P. D. Paulson, and V. Dutta, "Thin-Film Solar Cells: An Overview," Prog. Photovolt: Res. Appl., no 12 pp 69-92, 2004.

[15] T. Feurer *et al.*, "Progress in thin film CIGS photovoltaics – Research and development, manufacturing, and applications," *Prog. Photovoltaics Res. Appl.*, vol. 25, no. 7, pp. 645–667, Jul. 2017.

[16] D. Rudmann, A. F. da Cunha, M. Kaelin, F.-J. Haug, H. Zogg, and A. N. Tiwari, "Effects of Na on The Growth of Cu(In, Ga)Se $_2$ Thin Films and Solar Cells," *MRS Proc.*, vol. 763, p. B1.9, Feb. 2003.

[17] P. M. P. Salomé, H. Rodriguez-Alvarez, and S. Sadewasser, "Incorporation of alkali metals in chalcogenide solar cells," *Solar Energy Materials and Solar Cells*, vol. 143. Elsevier B.V., pp. 9–20, Jul. 2015.

[18] K. H. Ong *et al.*, "Review on substrate and molybdenum back contact in CIGS thin film solar cell," *International Journal of Photoenergy*, vol. 2018. Hindawi Limited, 2018.

[19] R. Scheer and H. W. Schock, *Chalcogenide Photovoltaics: Physics, Technologies, and Thin Film Devices*. Wiley-VCH, 2011.

[20] T. S. Lopes *et al.*, "Rear Optical Reflection and Passivation Using a Nanopatterned Metal/Dielectric Structure in Thin-Film Solar Cells," *IEEE J. Photovoltaics*, 2019.

[21] J. Schöldström, "Thermal Radiation from Co-evaporated Cu(In,Ga)Se2 : End point detection and process control,"Doctoral Dissertation, Uppsala Universitet, 2012.

[22] S. R. Thomas *et al.*, "Recent developments in the synthesis of nanostructured chalcopyrite materials and their applications: A review," *RSC Advances*, vol. 6, no. 65. Royal Society of Chemistry, pp. 60643–60656, 2016.

[23] J. Kessler, C. Chityuttakan, J. Lu, J. Schöldström, and L. Stolt, "Cu(In,Ga)Se_2 thin films grown with a Cu-poor/rich/poor sequence: Growth model and structural considerations," *Prog. Photovoltaics Res. Appl.*, vol. 11, no. 5, pp. 319–331, Aug. 2003.

[24] R. Kotipalli, B. Vermang, V. Fjällström, M. Edoff, R. Delamare, and D. Flandre, "Influence of Ga/(Ga+In) grading on deep-defect states of Cu(In,Ga)Se_2 solar cells," *Phys. Status Solidi - Rapid Res. Lett.*, vol. 9, no. 3, pp. 157–160, Mar. 2015.

[25] P. Szaniawski, "From Light To Dark: Electrical Phenomena in Cu(In,Ga)Se_2 Solar Cells" Doctoral Dissertation, Uppsala Universitet, 2009.

[26] J. Lindahl, "Atomic layer deposition of zinc tin oxide buffer layers for Cu(In,Ga)Se_2 Solar Cells" Doctoral Dissertation, Uppsala Universitet, 2015.

[27] J. Lindahl *et al.*, "Inline Cu(In,Ga)Se_2 co-evaporation for high-efficiency solar cells and modules," *IEEE J. Photovoltaics*, vol. 3, no. 3, pp. 1100–1105, 2013.

[28] J. Posada, M. Jubault, and N. Naghavi, "Ultra-thin Cu(In,Ga)Se_2 solar cells prepared by an alternative hybrid co-sputtering/evaporation process," *Thin Solid Films*, vol. 633, pp. 66–70, Jul. 2017.

[29] C. Colin *et al.*, "Ultrathin CIGS Solar Cells with Metallic Nanoparticles," *26th Eur. Photovolt. Sol. Energy Conf. Exhib.*, pp. 2863–2866, 2011.

[30] J. M. V. Cunha *et al.*, "Insulator Materials for Interface Passivation of Cu(In,Ga)Se_2 Thin Films," *IEEE J. Photovoltaics*, vol. 8, no. 5, pp. 1313–1319, Sep. 2018.

[31] P. M. P. Salomé *et al.*, "Passivation of Interfaces in Thin Film Solar Cells: Understanding the Effects of a Nanostructured Rear Point Contact Layer," *Adv. Mater. Interfaces*, vol. 5, no. 2, Jan. 2018.

[32] G. Birant, J. de Wild, M. Meuris, J. Poortmans, and B. Vermang, "Dielectric-based rear surface passivation approaches for Cu(In,Ga)Se_2 solar cells: A review," *Applied Sciences (Switzerland)*, vol. 9, no. 4. MDPI AG, Feb. 2019.

[33] D. Derkacs, S. H. Lim, P. Matheu, W. Mar, and E. T. Yu, "Improved performance of amorphous silicon solar cells via scattering from surface plasmon polaritons in nearby metallic nanoparticles," *Appl. Phys. Lett.*, vol. 89, no. 9, 2006.

[34] P. D. Paulson, R. W. Birkmire, and W. N. Shafarman, "Optical characterization of $CuIn_{1-x}Ga_xSe_2$ alloy thin films by spectroscopic ellipsometry," *J. Appl. Phys.*, vol. 94, no. 2, pp. 879–888, Jul. 2003.

[35] Q. Huang, X. Hu, Z. Fu, and Y. Lu, "Plasmonic Thin Film Solar Cells," in *Nanostructured Solar Cells*, InTech, 2017.

[36] C. Sun and X. Wang, "Efficient Light Trapping Structures of Thin Film Silicon Solar Cells Based on Silver Nanoparticle Arrays," *Plasmonics*, vol. 10, no. 6, pp. 1307–1314, Dec. 2015.

[37] G. Yin *et al.*, "Integration of plasmonic Ag nanoparticles as a back reflector in ultra-thin Cu(In,Ga)Se_2 solar cells," *Appl. Surf. Sci.*, vol. 355, pp. 800–804, Nov. 2015.

[38] M. J. Mendes, S. Morawiec, F. Simone, F. Priolo, and I. Crupi, "Colloidal plasmonic back reflectors for light trapping in solar cells," *Nanoscale*, vol. 6, no. 9, pp. 4796–4805, May 2014.

[39] S. Morawiec *et al.*, "Broadband photocurrent enhancement in a-Si:H solar cells with plasmonic back reflectors," *Opt. Express*, vol. 22, no. S4, p. A1059, Jun. 2014.

[40] B. V. Enüstün and J. Turkevich, "Coagulation of Colloidal Gold," *J. Am. Chem. Soc.*, vol. 85, no. 21, pp. 3317–3328, Nov. 1963.

[41] K. R. Brown, D. G. Walter, and M. J. Natan, "Seeding of colloidal Au nanoparticle solutions" *Chem. Mater.*, vol. 12, no. 2, pp. 306–313, Feb. 2000.

[42] A. Teixeira *et al.*, "Microfluidics-driven fabrication of a low cost and ultrasensitive SERS-based paper biosensor," *Appl. Sci.*, vol. 9, no. 7, Apr. 2019.

[43] FDTD Solutions Lumerical Software Manual, 2011. URL: http://www.lumerical.com/products/fdtd/ [Acessed: 15-09-2019].

[44] R. E. Treharne, A. Seymour-Pierce, K. Durose, K. Hutchings, S. Roncallo, and D. Lane, "Optical design and fabrication of fully sputtered CdTe/CdS solar cells," in *Journal of Physics: Conference Series*, vol. 286, no. 1, 2011.

[45] C. Stelling, C. R. Singh, M. Karg, T. A. F. König, M. Thelakkat, and M. Retsch, "Plasmonic nanomeshes: Their ambivalent role as transparent electrodes in organic solar cells," *Sci. Rep.*, vol. 7, Feb. 2017.
[46] E. D. Palik, *Handbook of Optical Constants of Solids, Five-Volume Set*. Elsevier Science, 1997.
[47] P. B. Johnson and R. W. Christy, "Optical constants of the noble metals," *Phys. Rev. B*, vol. 6, no. 12, pp. 4370–4379, 1972.
[48] W. S. M. Werner, K. Glantschnig, and C. Ambrosch-Draxl, "Optical constants and inelastic electron-scattering data for 17 elemental metals," *J. Phys. Chem. Ref. Data*, vol. 38, no. 4, pp. 1013–1092, 2009.
[49] "Mie Scattering 3D (FDTD)." [Online]. Available: https://apps.lumerical.com/particle_scattering_mie_3d.html. [Accessed: 17-Sep-2019].
[50] M. J. Mendes *et al.*, "Design of optimized wave-optical spheroidal nanostructures for photonic-enhanced solar cells," *Nano Energy*, vol. 26, pp. 286–296, Aug. 2016.
[51] A. R. Shafiqa, A. Abdul Aziz, and B. Mehrdel, "Nanoparticle Optical Properties: Size Dependence of a Single Gold Spherical Nanoparticle," in *Journal of Physics: Conference Series*, vol. 1083, no. 1, 2018.
[52] M. A. Garcia, "Surface plasmons in metallic nanoparticles: Fundamentals and applications," *Journal of Physics D: Applied Physics*, vol. 44, no. 28, Jul. 2011.
[53] W. L. Barnes, "Particle Plasmons: Why Shape Matters." *American Journal of Physics* 84, 593, 2016
[54] K. Islam, A. Alnuaimi, E. Battal, A. K. Okyay, and A. Nayfeh, "Effect of gold nanoparticles size on light scattering for thin film amorphous-silicon solar cells," *Sol. Energy*, vol. 103, pp. 263–268, 2014.
[55] V. Amendola, R. Pilot, M. Frasconi, O. M. Maragò, and M. A. Iatì, "Surface plasmon resonance in gold nanoparticles: A review," *Journal of Physics Condensed Matter*, vol. 29, no. 20. Institute of Physics Publishing, Apr. 2017.
[56] S. A. Maier, "*Plasmonics: Fundamentals and applications*." Springer US, 2007.
[57] P. B. Johnson *et al.*, "Plasmonic nanoparticle enhanced light absorption in GaAs solar cells," *Applied Physics Letters*, 93(12), 121904, Sept. 2008.
[58] S. Hrapovic, Y. Liu, G. Enright, F. Bensebaa, and J. H. T. Luong, "New strategy for preparing thin gold films on modified glass surfaces by electroless deposition," *Langmuir*, vol. 19, no. 9, pp. 3958–3965, Apr. 2003.
[59] "Poly(diallyldimethylammonium chloride) solution | Sigma-Aldrich." [Online]. Available: https://www.sigmaaldrich.com/catalog/substance/polydiallyldimethylammoniumchloridesolution123452606279311?lang=pt&region=PT. [Accessed: 19-Sep-2019].
[60] C.-C. Chiang *et al.*, "Optical tweezers based active microrheology of sodium polystyrene sulfonate (NaPSS)," *Opt. Express*, vol. 19, no. 9, p. 8847, Apr. 2011.
[61] M. A. Green, "The Passivated Emitter and Rear Cell (PERC): From conception to mass production," *Sol. Energy Mater. Sol. Cells*, vol. 143, pp. 190–197, Jul. 2015.
[62] S. Bose *et al.*, "A morphological and electronic study of ultrathin rear passivated Cu(In,Ga)Se2 solar cells," *Thin Solid Films*, vol. 671, pp. 77–84, Feb. 2019.
[63] A. Čampa, J. Krč, J. Malmström, M. Edoff, F. Smole, and M. Topič, "The potential of textured front ZnO and flat TCO/metal back contact to improve optical absorption in thin Cu(In,Ga)Se2 solar cells," *Thin Solid Films*, vol. 515, no. 15 SPEC. ISS., pp. 5968–5972, May 2007.
[64] N. Dahan *et al.*, "Optical approaches to improve the photocurrent generation in Cu(In,Ga)Se2 solar cells with absorber thicknesses down to 0.5 μm," *J. Appl. Phys.*, vol. 112, no. 9, Nov. 2012.
[65] F. Mollica, "Optimization of ultra-thin Cu(In,Ga)Se 2 based solar cells with alternative back-contacts" Chemical Physics, Université Pierre et Marie Curie - Paris VI, 2016.
[66] R. Scheer, "Towards an electronic model for CuIn1 - XGaxSe 2 solar cells," in *Thin Solid Films*, vol. 519, no. 21, pp. 7472–7475, 2011.
[67] S. J. C. Irvine, "Photovoltaic (PV) thin-films for solar cells," in *Functional Materials for Sustainable Energy Applications*, Elsevier Ltd, pp. 22–41, 2012.
[68] L. Scarabelli, M. Grzelczak, and L. M. Liz-Marzán, "Tuning gold nanorod synthesis through prereduction with salicylic acid," *Chem. Mater.*, vol. 25, no. 21, pp. 4232–4238, Nov. 2013.

6 Annex

6.1 Annex 1: Au NPs solution characterization

The synthetized Au NP colloidal solutions were characterized through their absorption spectrum, which are represented on **Figure 6.1**.

Through the absorption spectrum an estimate of the Au NP solution concentration can be made. The concentration of the Au NP solution can be de determined through the absorption value at 400 nm, since at this wavelength value interband transitions are dominant, and therefore, the absorption at 400 nm is independent on the particles shape and size [68].

Assuming a complete reduction of Au, an absorbance of 1.2 at 400 nm (ABS_{400} = 1.2) can be related to a concentration (*C*) of 0.5 mM, according to [68].Through the beer-lambert law, the Au molar extinction coefficient (*k*) can then be calculated through:

$$ABS_{400} = k \times L \times C$$

where *L* is the optical path length in cm. Considering a *L* of 1 cm, the ABS_{400} at 1.2 and a *C* of 0.5 mM the molar extinction coefficient of gold can then be calculated:

$$k = \frac{ABS_{400}}{L \times C} = 2.4 \times 10^{-3} M^{-1} cm^{-1}$$

With a *k* value of 2.4×10^{-3} the concentration of the synthetized solutions can then be calculated through the beer-lambert law considering the measured ABS_{400}.

The size of the Au NPs was later confirmed through the analysis of SEM images. The Au NP solution concentration and the average radius of the Au NPs in each synthesis measured through the SEM analysis using the imagej software are represented in **Table 6.1**.

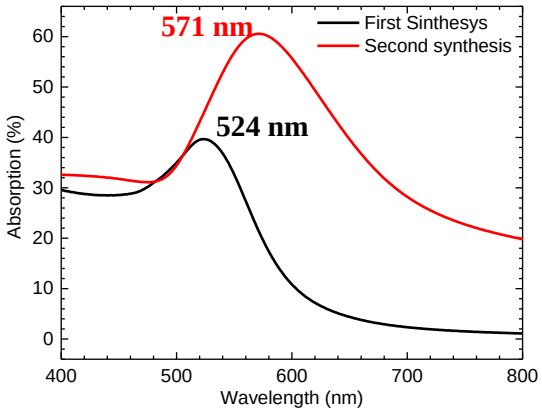

Figure 6.1 - Absorption spectrum of the first synthesized Au colloidal solution (black), and the second synthesized Au colloidal solution (red).

Table 6.1 - Averages and standard deviations of the results from the Au NPs solution analysis.

Synthesis	Au concentration (mM)	NP radius (nm)
First	0.12	12.31±1.90
Second	0.14	59.12±13.06

6.2 Annex 2: Supplementary figures

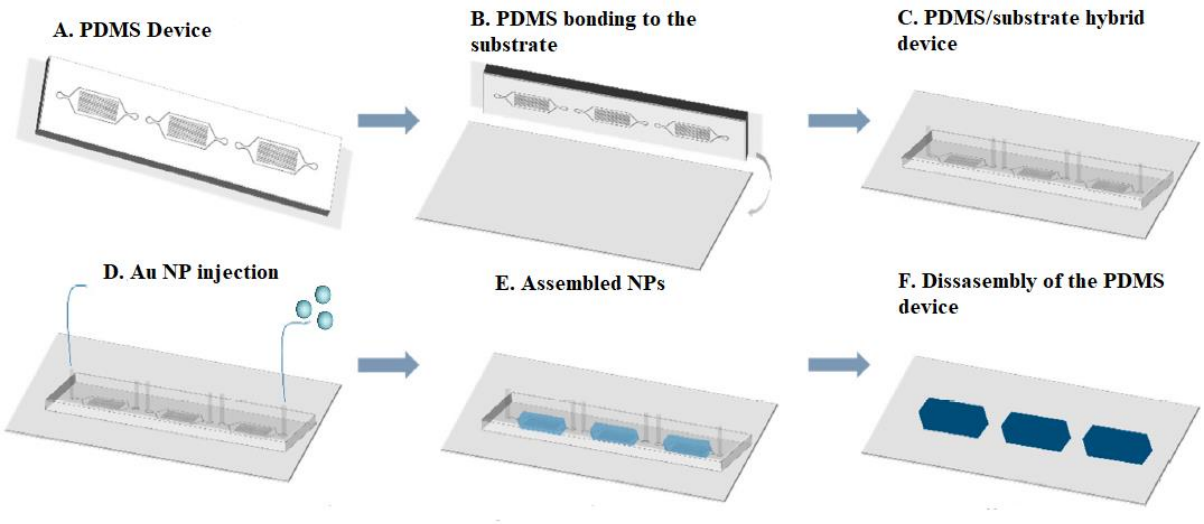

Figure 6.2 - Schematic representation of the experimental protocol for the Au NPs deposition with the PDMS device. Adapted from [42].

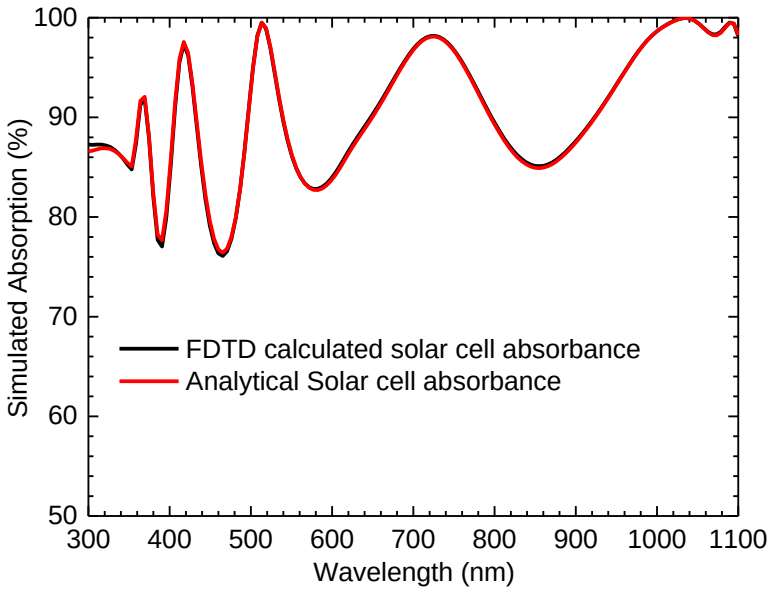

Figure 6.3 - Comparison between the FDTD simulated result and the Transfer Matrix analytical formalism. The curves represented in this image are from the regular 2 µm solar cell.

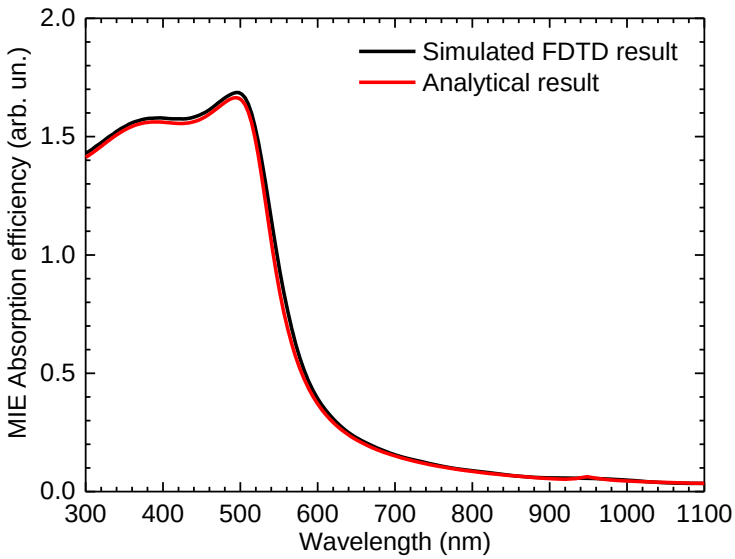

Figure 6.4 - Comparison between the simulated FDTD result and the theoretical solution. Both the represented curves are from the NP with a radius of 100 nm.

6.3 Annex 3: Solar cell characterization – Advanced parameters

Table 6.2 - Averages and standard deviations of the solar cell's advanced parameters.

Sample	R_p (Ω)	R_s (Ω)	A
MOAL	187.3±116.4	12.2±2.5	1.8±0.4
SI	154.6±56.6	17.7±5.3	1.8±0.2
MOSI	513.7±271.4	14.7±6.2	2.4±0.5
ALPASS	382.2±104.7	9.5±3.4	1.7±1.0
SIPASS	301.8±62.2	9.63±0.9	1.5±0.4
REF 1	399.9±208.5	10.0±5.2	1.5±0.5
REF 2	206.1±89.2	10.9±4.0	1.4±0.3

6.4 Annex 4: Journal Publication

J. M. V. Cunha *et al.,* "Decoupling of Optical and Electrical Properties of Rear Contact CIGS Solar Cells", *IEEE Journal of Photovoltaics*, 2019. DOI: 10.1109/JPHOTOV.2019.293335

***Abstract*—A novel architecture that comprises rear interface passivation and increased rear optical reflection is presented with the following advantages: i) enhanced optical reflection is achieved by the deposition of a metallic layer over the Mo rear contact; ii) improved interface quality with CIGS by adding a sputtered Al_2O_3 layer over the metallic layer; and, iii) optimal ohmic electrical contact ensured by rear-openings refilling with a second layer of Mo as generally observed from the growth of CIGS on Mo. Hence, a decoupling between the electrical function and the optical purpose of the rear substrate is achieved. We present in detail the manufacturing procedure of such type of architecture together with its benefits and caveats. A preliminary analysis showing an architecture proof-of-concept is presented and discussed.**

***Index Terms*—Cu(In,Ga)Se_2 (CIGS), passivation, semiconductors, ultrathin.**

I. Introduction

Nowadays, absorber layers of Cu(In,Ga)Se_2 (CIGS) with sub-micrometer thicknesses, or ultrathin absorbers, are one of the main thin-film solar cell research topics. In addition to a lower material cost due to its usage reduction, the bulk recombination rate within the CIGS absorber layer may also decrease [1]–[3]. With these two potential benefits, research work has been focused on solving two inherent problems entailed by the use of ultrathin photovoltaic technology: i) increased rear interface recombination at the Mo/CIGS interface, and ii) abridged photogeneration due to the necessary width for full absorption being effectively larger than the absorber thickness. In other words, the light path is significantly shorter than the absorption length. Despite the presence of rear interface recombination in thick films, the effect is more pronounce in ultrathin devices. Such recombination losses are higher in ultrathin devices as a larger share of the minority charge carriers are generated closer to the rear contact as compared with standard thick CIGS devices. A solution to mitigate such problems is the use of a structure located between the rear contact and the CIGS layer comprising a dielectric passivation layer with point contacts [1], [4]–[7]. The main limitation of this approach is that the point contacts need to occupy an area as small as possible, while, at the same time, being located within distances close enough to avoid resistive losses [8]. This compromise means that the gap between two contacts needs to be in a range of 1–4 μm. In order to decrease the contact area, the opening diameters should be limited from 100 to 400 nm. Hence, recent works have been dealing with the determination of the most suitable dielectric material to be used among Al_2O_3, SiO_2, Si_3N_4, HfO_2, etc. [1], [5], [6], [9] as well as with the determination of the most suitable patterning approach [4], [6], [10]–[12]. Until now, e-beam lithography of atomic layer deposited (ALD) Al_2O_3 has been the benchmark of the performed studies [4], and optical lithography of line contacts has shown positive results with the benefit of being more industrial friendly [8]. With regards to optical losses, several approaches have been tested with different outcomes. Z. J. Li-Kao *et al.* [13] developed an ingenious but complex CIGS lift-off process that moves the CIGS into an Au substrate allowing for an ohmic contact with excellent reflective properties [14], [15]. However, the procedure seems to be very complex for industrial application. The replacement of Mo by other metals with higher reflection is yet to be achieved mostly due to metal out-diffusion to the CIGS, selenization of the metal, or poor electrical contact [16], [17]. Moreover, part of the difficulty with the increase off the rear optical reflection is related to the coupling of the optical property of this layer with the electrical contacts. Empirically, Mo is known to be the unique solution [18] due, among other things, to the suppression of Se diffusion and the formation of a very thin MoSe2 layer, enhancing a good ohmic contact [19]. Hence, an ideal rear contact architecture for ultrathin CIGS solar cells would need to have:

i) Mo as the electrical contact;
ii) high optical reflection; and
iii) an additional passivation strategy.

For these objectives to be met, a decoupling of the optical properties with the electrical properties of the rear contact is required. In this work, we present a process that merges the Mo point contact structure with a metal reflective layer. This approach ensures that the contacts occupying a small percentage of the interface area are made of Mo, allowing for a good ohmic contact. The rest of the area is left with the passivation material and underneath a highly reflective material that further reduces the optical losses of ultrathin devices. Furthermore, Mo will prevent Se diffusion into the metallic interlayers, and, therefore, serve also as a diffusion barrier.

II. Experimental

In this section, we will present the fabrication procedure of the studied devices with the exception of the new architecture that will be presented in detail in the next section. The standard CIGS solar cell stack is soda-lime-glass (SLG)/Mo/CIGS/CdS/i:ZnO/ZnO:Al with Ni/Al/Ni as front contacts [20]. With the exception of our reference device, an evaporated 15-nm sodium fluoride (NaF) precursor layer was deposited on the top of the rear contact structure just prior to the CIGS

growth [21]. The average thickness of the CIGS layer, which was measured using stylus profilometry, is (0.62 ± 0.05) μm with the compositional values of [Cu]/([Ga]+[In])=0.88 ± 0.02 and [Ga]/([Ga]+[In])=0.31 ±0.01, which was measured using X-ray fluorescence. Ungraded (flat profile evaporation rates) CIGS absorbers were used for our experiments [4], [22],[23], with a growth temperature of 550 °C. The metal diffusion can be significant due to the high processing temperature used during the CIGS growth. Twelve individual solar cells were defined with an area of 0.5 cm_2, as described elsewhere [20]. To study the electrical behavior of the solar cells, illuminated current density versus voltage (J–V) at AM1.5 and external quantum efficiency (EQE) measurements were performed in home-built systems. Simulations of the solar cells were done using a numerical three-dimensional mesh-based finite-difference time-domain (FDTD) method to model the optical response of the fabricated structures, employing a specialized commercial solver [4], [17]. A focused ion beam, Helios NanoLab 450s from FEI, was used to prepare the cross-section samples for the transmission electron microscopy (TEM) analysis. The lamella polishing was finished with a low Ga-ion accelerating voltage, below 2 kV. The TEM study was performed at 200 kV on a Titan (G3) Cubed Themis from FEI, utilizing the software Esprit from Bruker. The samples description and name used hereafter are presented in Table I. A reference ultrathin (A) and a passivation reference (B) were fabricated. Moreover, to validate the benefits of the lift-off process, two samples with a Ta interlayer were produced. One sample with a simple Ta interlayer, Mo/Ta/Al_2O_3 (sample C), is studied.Asecond sample with the lift-off process, where Ta is the interlayer and in addition there is Mo inside the line contacts (sample D), is also studied, as depicted in Fig. 1.

III. Proposed Architecture and Processing Steps

The novel architecture is schematically shown in Fig. 1. For a proof-of-concept, we use line contacts instead of point contacts, as the point contact process is more complex and time-consuming, and the line contacts are industrially scalable using conventional optical lithography. The dimensions of the lines and their spacing can lead easily to contact resistance losses (seen in V_{oc} and FF losses) and, therefore, their design requires special attention [8]. Hence, 700 nm lines spaced by a 2.8 μm pitch are used in this article, as they are known to reduce the rear-interface recombination velocity [8]. We will use Ta as the interlayer for several reasons:

TABLE I
Samples Description and Respective Naming

Substrate	Description
SLG/Mo	(A) Mo reference
SLG/Mo/ns-Al_2O_3	(B) Passivation reference
SLG/Mo/Ta/ns-Al_2O_3	(C) Ta interlayer
SLG/Mo/Ta/ns-Al_2O_3/Mo	(D) Lift-off process with Mo filling the contacts

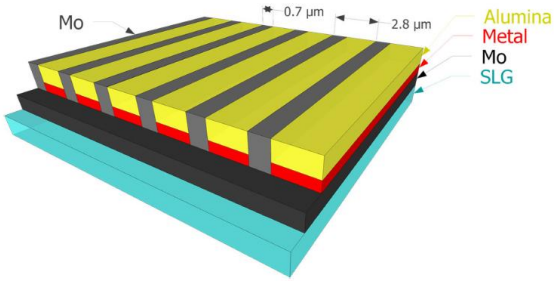

Fig. 1. Schematic representation of the developed architecture with Mo filling the line contacts.

i) theoretically, as shownin Section IV-B, it has the potential to reflect more light than the standard structure;
ii) if not fully encapsulated, it will heavily degrade CIGS performance through elemental in- and out-diffusion [7];
and
iii) we can etch vertical structures inside Ta using the same reactive ion etching procedure used for the opening of the Al_2O_3 structures.

The photolithography steps necessary for the substrate fabrication are depicted in Fig. 2 and commented in Table II. The lithographic definition is done using optical lithography, and the Al2O3 is open with a reactive ion etch step. Ideally, the etching opens both the Al2O3 and the metal layer. At this point, the photoresist is kept, and the second-Molayer is deposited. The lift-off allows for Mo to be kept inside the line contacts leaving the Al2O3 layer exposed.

IV. Results

A. Morphological Analysis

To demonstrate that the lift-off process used in sample D: i) prevents Se diffusion; and ii) allows for the contact lines to be cleaned from Al_2O_3 and Ta, we performed EDS analysis in a TEM cross-section image. Fig. 3 shows the EDS maps for Mo, Al, Ta, Se, and Cu. The EDS analysis was performed at the border between a line contact and the Ta/Al_2O_3 insulated area. The analysis shows:
i) there is no Se diffusion into the Al_2O_3, or inside the line contact, demonstrating that the second Mo layer prevents Se diffusion;
ii) the lift-off Mo layer inside the line contact superimposes the line edge, further preventing lateral diffusion; and
iii) the etching process fully removes Al from the line contact allowing for electrical contact.

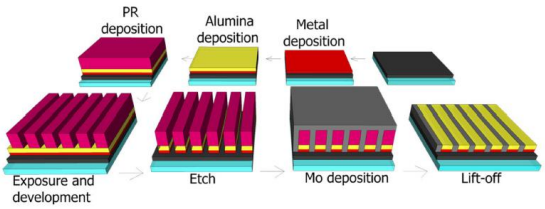

Fig. 2. Schematic representation of the photolithography process used for the formation of the line contacts and the deposition of Mo inside. PR is an acronym for Photoresist.

TABLE II
DETAILED DESCRIPTION OF THE CLEAN ROOM PROCESSING OF THE LIFT-OFF PROCESS THAT PROVIDES FOR A LINE CONTACT STRUCTURE FILLED WITH Mo

Step	Description	Properties
0	SLG substrate	Cleaning by ultrasounds and detergent in H_2O
1	Mo rear contact deposition	Bilayer Mo, DC-sputtering - 350 nm total thickness
2	Metallic layer deposition	DC Sputtering - 10 nm
3	Passivation layer deposition	RF sputtering - 18 nm
4	Contact lines creation by direct laser write exposure	• HMDS (hexamethyldisilazane) vapor priming • Deposition of photoresist by spin coating • Laser exposure • Pattern development
5	Opening of the contact lines	Dry etching using reactive ion etching (ICP)
6	Mo deposition in the lines	DC-Sputtering - 30 nm
7	Lift-off	Ultrasounds in an acetone bath
8	Surface cleaning	O_2 Plasma treatment
9	Solar cell fabrication	Angstrom Solar cell Baseline [20]

This analysis, in particular, leaves open the possibility that some Ta remains inside the line contact. Despite considering that these Ta residues form a very thin layer trapped in-between Mo, we performed an EDS line scan in the middle of the line contact. The EDS line scan measurements for outside the line contact and inside the line, respectively, are shown in Figs. 4 and 5. Both EDS line scans show very well-defined structures, which withstood the harsh CIGS co-evaporation process. Furthermore, Fig. 5 shows no presence of Ta in the line contact, evidencing that we have the expected Mo/Mo/CIGS structure. Thus, an effective etching of Ta and Al_2O_3 and a successful second Mo deposition have been performed. We note that both analyses, and also the EDS mapping show a residual amount of Mo in the CIGS. Nonetheless, it is only a background signal emanating from the Mo TEM grid used for the study.

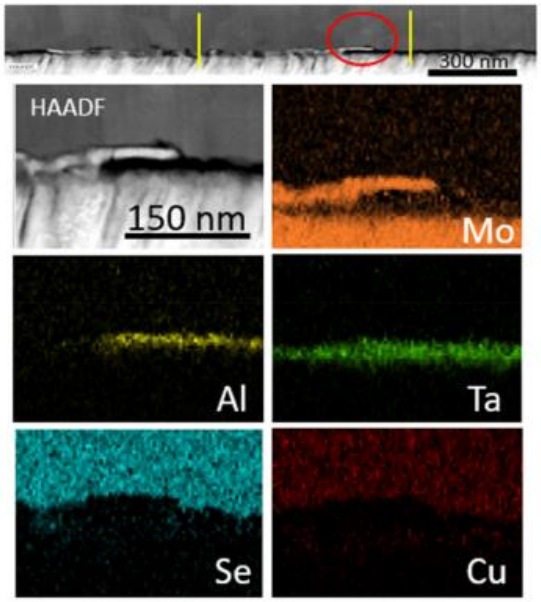

Fig. 3. TEM high angular annular dark-field image (HAADF) cross-section image and EDS mapping of sample D. The red circle corresponds to the EDS mapping area, whereas the vertical yellow lines correspond to the line scan regions.

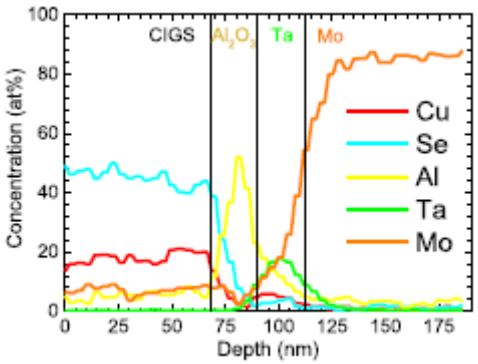

Fig. 4. EDS line scan passivated Mo/Ta/Al_2O_3/CIGS. The vertical lines are guides represent the layered passivation structure.

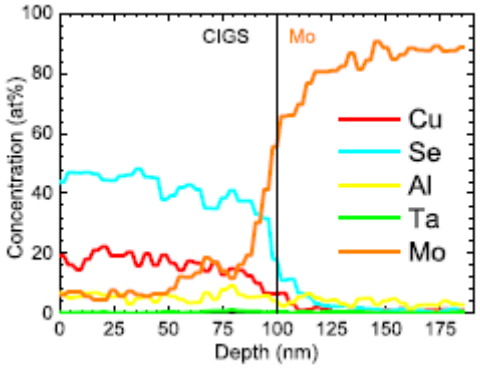

Fig. 5. EDS line scan Mo/CIGS inside line contact. The vertical lines represent the well-defined Mo/CIGS line contact.

B. Electrical Characterization

The *J–V* measurements are depicted in Fig. 6, and respective figures of merit are shown in Table III. Both *J–V* and EQE results (see Fig. 7) confirm the benefits of employing rear passivation by comparing a Mo reference (sample A) with a passivation reference (sample B), as expected and widely reported [1], [4], [6], [10], [17], [24]–[26].

Although the reference sample (A) shows a low average efficiency (5.4%), it is within the range of values presented in the literature. Ultrathin CIGS devices need different optimizations than the ones of regular CIGS thickness, and this fact causes runs to be more variable than their thick counterparts. Sample A also shows evidence of voltage-dependent current collection (VDCC) and/or shunting, which is common in ultrathin CIGS solar cells. Such problems are explained in more detail elsewhere [4]. As such, the reference sample (A) has a low fill factor (FF), which is recovered by the passivation reference (B), with shunts mitigation by the passivation layer. We observe that sample D features the highest values of V_{oc}, FF, and efficiency, reaching an average light to power conversion efficiency of 9.6%. Such value is 4.2% (abs) higher than the reference sample and 2.4% (abs) higher than the passivation reference. The V_{oc} value of sample D is 24 mV higher than the passivation reference; hence, the passivation effect is still present and reinforced. Furthermore, there seems to be a J_{sc} improvement of 0.25 mA/cm2, which may be related to an increased reflection achieved by the employment of the tantalum material and that will be discussed further in the text. To demonstrate the importance of the Mo second layer deposited in the line contacts, we also produced sample C that allows Se to be in direct contact with Ta. Sample C shows poor solar cell results, most likely due to diffusion of elements and/or a poor electrical contact between Ta and CIGS, showing the importance of the lift-off process used for sample D. This comparison highlights the importance of a diffusion barrier, also in accordance with previous results [16], [17]. The champion cell of sample D achieved an efficiency value of 10.0%. Moreover, sample D shows an excellent diode-like behavior, with the lowest dark current (J_0) value ($\sim 4 \times 10^{-6}$ mA/cm2), and no evidence of either shunting, seen by the high shunt resistance value, or roll-over effects, which is demonstrated by its high FF value (~70%).

C. Optical Simulations

To better understand the optical gains of using Ta underneath the passivation layer, we will proceed with an optical simulation of the novel stack, shown in Fig. 1, and compare it with the EQE results presented in Fig. 7 for the most important samples identified previously (A, B, and D). It is noted that the optical simulations performed do not account for electrical losses, light scattering in grain boundaries, doping and compositional CIGS variations, interface smearing, just to name a few parameters that influence real devices. Therefore, a difference is expected between the simulated values and the measured ones. Nonetheless, the optical simulations presented in Fig. 8 are in good agreement with

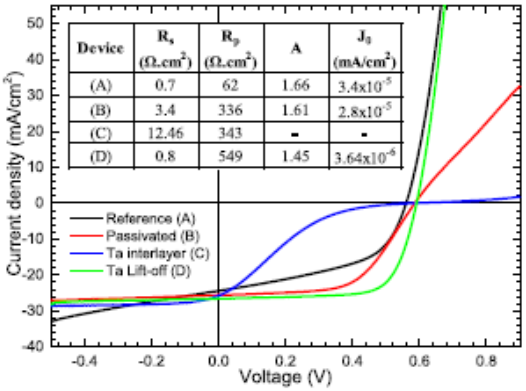

Fig. 6. Illuminated *J–V* curves of the highest V_{oc} device for all samples. The diode parameters are found on the inset table.

TABLE III
J–V VALUES AVERAGES AND STANDARD DEVIATION OF TWELVE DEVICES FOR EACH SUBSTRATE TYPE

Sample	V_{oc} (mV)	EQE corrected J_{sc} (mA/cm²)	FF (%)	Eff (%)
(A)	535 ± 11 (560)	21.37 ± 0.32 (21.82)	47.5 ± 4.6 (49.9)	5.4 ± 0.7 (6.4)
(B)	558 ± 23 (586)	23.13 ± 0.18 (23.46)	55.2 ± 2.5 (58.5)	7.2 ± 0.7 (8.2)
(C)	519 ± 41 (579)	24.35 ± 0.71 (24.96)	14.5 ± 2.0 (15.7)	1.8 ± 0.2 (2.2)
(D)	582 ± 5 (591)	23.38 ± 0.29 (23.59)	68.0 ± 3.4 (71.7)	9.6 ± 0.5 (10.0)

Note. The values in parenthesis are for the highest V_{oc} device.

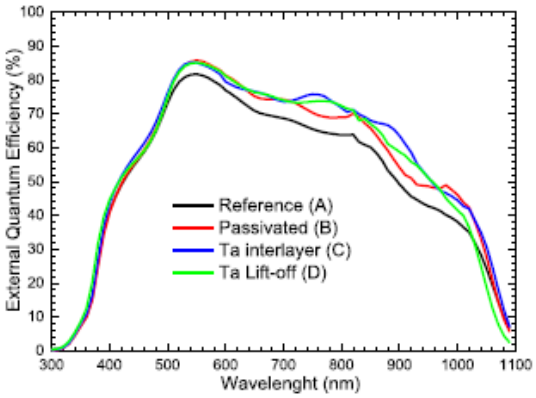

Fig. 7. EQE of the studied samples.

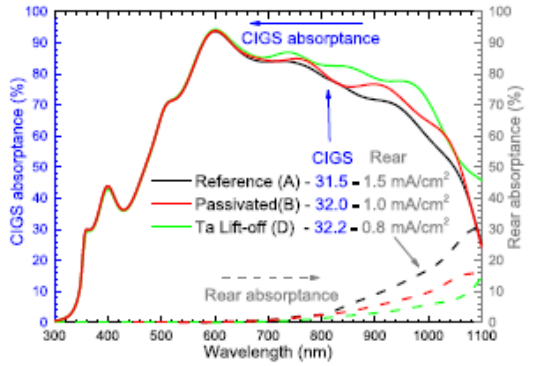

Fig. 8 Simulated CIGS absorptance and rear contact absorptance. For sample A, rear contact absorptance is theMoabsorptance; for sample B, it isMo+Al2O3 absorptance; and for sample D, it is the absorptance of Mo+Ta+Al2O3+Mo.

the EQE, even confirming that by adding the passivation layer, an optical effect leads to an increase in the J_{sc} values. However, the experimental J_{sc} difference between A and B (1.76 mA/cm^2) is higher than the simulated J_{sc} difference (0.5 mA/cm^2). Such inconsistency is an evidence that part of the J_{sc} increase in sample B is due to electrical passivation and that further passivation optimization is needed. This fact is also highlighted by the observation that in the absorption calculations, there is no difference between the samples behaviour in the short wavelength regime contrary to what is observed in the EQE results, where the samples with passivation present a higher performance even where no optical gains are expected. Such increase in the EQE behavior in all wavelength values, when a passivation layer is added, is observed throughout the literature and needs to be studied in detail.We also note that the experimental J_{sc} difference between B and D (0.25 mA/cm^2) is very close to the simulated J_{sc} value (0.2 mA/cm^2). This is an indication that the passivation is the same in both substrates and that the simulation is in agreement with the experimental results. Furthermore, by using the novel architecture of sample D, a decrease in parasitic absorption at the rear contact is observed, as shown by the dashed lines in Fig. 8. According to the simulations and with regard to parasitic absorption in the rear contact, sample A has a J_{sc} loss of 1.53 mA/cm^2 in the Mo layer, sample B has a J_{sc} loss of 1.03 mA/cm2 in the Mo+Al_2O_3 layer and, remarkably, sample D has a J_{sc} loss of 0.86 mA/cm2 in the Mo+Ta+Al_2O_3+Mo. Such solution that allows for a decrease in parasitic absorption at the rear contact is highly interesting even for standard thickness CIGS (2000 nm), where the Mo absorptance can also reach values higher than 1 mA/cm^2 [27]. We note that for high reflective metals, other losses that are already present here become even more prominent, namely reflection losses, bringing the need to incorporate more advanced light-trapping mechanisms. Nonetheless, even with the improved novel architecture, the J_{sc} values are still far away from simulated values, likely meaning that not only light trapping has to be improved, but also the interface recombination velocity has to be further reduced.

V. Conclusion

In this preliminary study, we introduced a lift-off procedure to fabricate a substrate for thin-film solar cells that decouples the electrical properties from the optical ones. This is accomplished by the electrical contact being made between CIGS and a Mo line contact that uses only a part of the available rear contact area. The rest of the area is passivated by an Al_2O_3 layer, which underneath can have a highly reflective metal layer. Solar cells with the novel lift-off process using Ta as an interlayer show an improvement over both the reference devices and the substrates with Ta without the lift-off process. The 600-nm CIGS thickness solar cells with the new rear contact architecture achieved an average efficiency of 9.6%, which compares to the unpassivated reference of 5.4%.

The proposed novel architecture allows for:
1) a good electrical contact between the CIGS and the rear contact;
2) a beneficial passivation effect;
3) a reduced rear contact light absorptance; and
4) a limitation to the diffusion from and to the absorber layer.

Such architecture allows for a wider ensemble of metals to be used to increase the rear optical reflectance, as most limitations of other metals can now be overcome. Future studies should be focused on studying the effects of this architecture, improving the lift-off process, and testing highly reflective metals.

References

[1] B. Vermang, V. Fjällström, J. Pettersson, P. Salomé, and M. Edoff, "Development of rear surface passivated Cu(In,Ga)Se_2 thin film solar cells with nano-sized local rear point contacts," *Sol. Energy Mater. Sol. Cells*, vol. 117, pp. 505–511, Oct. 2013.
[2] J. Krc *et al.*, "Optical confinement in chalcopyrite based solar cells," *Thin Solid Films*, vol. 633, pp. 193–201, Jul. 2017.
[3] J. M. V. Cunha, C. Rocha, C. Vinhais, P. A. Fernandes, and P. M. P. Salomé, "Understanding the AC equivalent circuit response of ultrathin Cu(In,Ga)Se_2 solar cells," *IEEE J. Photovolt.*, 2019, doi: 10.1109/JPHOTOV.2019.2927918.
[4] P. M. P. Salomé *et al.*, "Passivation of interfaces in thin film solar cells: Understanding the effects of a nanostructured rear point contact layer," *Adv. Mater. Interfaces*, vol. 5, no. 2, Jan. 2018, Art. no. 1701101.
[5] B. Vermang *et al.*, "Employing Si solar cell technology to increase efficiency of ultra-thin Cu(In,Ga)Se_2 solar cells," *Prog. Photovolt. Res. Appl.*, vol. 22, no. 10, pp. 1023–1029, Oct. 2014.
[6] G. Yin *et al.*, "Well-controlled dielectric nanomeshes by colloidal nanosphere lithography for optoelectronic enhancement of ultrathin Cu(In,Ga)Se_2 solar cells," *ACS Appl. Mater. Interfaces*, vol. 8, no. 46, pp. 31646–31652, Nov. 2016.
[7] B. Vermang *et al.*, "Rear surface optimization of CZTS solar cells by use of a passivation layer with nanosized point openings," *IEEE J. Photovolt.*, vol. 6, no. 1, pp. 332–336, Jan. 2016.
[8] S. Bose *et al.*, "Optical lithography patterning of SiO_2 layers for interface passivation of thin film solar cells," *Sol. RRL*, vol. 2, no. 12, Dec. 2018, Art. no. 1800212.
[9] J. M. V. Cunha *et al.*, "Insulator materials for interface passivation of Cu(In,Ga)Se_2 thin films," *IEEE J. Photovolt.*, vol. 8, no. 5, pp. 1313–1319, Sep. 2018.
[10] S. Bose *et al.*, "A morphological and electronic study of ultrathin rear passivated Cu(In,Ga)Se_2 solar cells," *Thin Solid-Films*, vol. 671, pp. 77–84, Feb. 2019.
[11] S. Choi *et al.*, "Lithographic fabrication of point contact with Al_2O_3 rearsurface-passivated and ultra-thin Cu(In,Ga)Se_2 solar cells," *Thin Solid Films*, vol. 665, pp. 91–95, Nov. 2018.
[12] G. Yin, P. Manley, and M. Schmid, "Light trapping in ultrathin $CuIn_{1-x}Ga_xSe_2$ solar cells by dielectric nanoparticles," *Sol. Energy*, vol. 163, pp. 443–452, Mar. 2018.
[13] Z. J. Li-Kao *et al.*, "Towards ultrathin copper indium gallium diselenide solar cells: Proof of concept study by chemical etching and gold back contact engineering," *Prog. Photovolt. Res. Appl.*, vol. 20, no. 5, pp. 582–587, Aug. 2012.
[14] N. Naghavi *et al.*, "Ultrathin Cu(In,Ga)Se_2 based solar cells," *Thin Solid Films*, vol. 633, pp. 55–60, Jul. 2017.
[15] N. Dahan *et al.*, "Optical approaches to improve the photocurrent generation in Cu(In,Ga)Se_2 solar cells with absorber thicknesses down to 0.5 μm," *J. Appl. Phys.*, vol. 112, no. 9, Nov. 2012, Art. no. 094902.

[16] K. Orgassa, H. W. Schock, and J. H. Werner, "Alternative back contact materials for thin film Cu(In,Ga)Se_2 solar cells," *Thin Solid Films*, vol. 431–432, pp. 387–391, May 2003.
[17] T. S. Lopes *et al.*, "Rear optical reflection and passivation using a nanopatterned metal/dielectric structure in thin film solar cells," *IEEE J. Photovolt.*, 2019, doi: 10.1109/JPHOTOV.2019.2922323.
[18] P. M. P. Salomé, J. Malaquias, P. A. Fernandes, and A. F. da Cunha, "Mo bilayer for thin film photovoltaics revisited," *J. Phys. D. Appl. Phys.*, vol. 43, no. 34, Sep. 2010, Art. no. 345501.
[19] P. Salomé, V. Fjällström, A. Hultqvist, and M. Edoff, "Na doping of CIGS solar cells using low sodium-doped Mo layer," *IEEE J. Photovolt.*, vol. 3, no. 1, pp. 509–513, Jan. 2013.
[20] J. Lindahl *et al.*, "In line Cu(In,Ga)Se_2 co-evaporation for high-efficiency solar cells and modules," *IEEE J. Photovolt.*, vol. 3, no. 3, pp. 1100–1105, Jul. 2013.
[21] P. M. P. Salomé *et al.*, "Cu(In,Ga)Se_2 solar cells with varying Na content prepared on nominally alkali-free glass substrates," *IEEE J. Photovolt.*, vol. 3, no. 2, pp. 852–858, Apr. 2013.
[22] P. M. P. Salomé *et al.*, "The effect of high growth temperature on Cu(In,Ga)Se_2 thin film solar cells," *Sol. Energy Mater. Sol. Cells*, vol. 123, pp. 166–170, Apr. 2014.
[23] O. Lundberg, M. Edoff, and L. Stolt, "The effect of Ga-grading in CIGS thin film solar cells," *Thin Solid Films*, vol. 480–481, pp. 520–525, Jun. 2005.
[24] B. Vermang *et al.*, "Introduction of Si PERC rear contacting design to boost efficiency of Cu(In,Ga)Se_2 solar cells," *IEEE J. Photovolt.*, vol. 4, no. 6, pp. 1644–1649, Nov. 2014.
[25] M. Schmid, "Review on light management by nanostructures in chalcopyrite solar cells," *Semicond. Sci. Technol.*, vol. 32, no. 4, Apr. 2017, Art. no. 043003.
[26] G. Birant, J. de Wild, M. Meuris, J. Poortmans, and B. Vermang, "Dielectric-based rear surface passivation approaches for Cu(In,Ga)Se_2 solar cells—A review," *Appl. Sci.*, vol. 9, no. 4, Feb. 2019, Art. no. 677.
[27] B. Bissig *et al.*, "Novel back contact reflector for high efficiency and double-graded Cu(In,Ga)Se_2 thin-film solar cells," *Prog. Photovolt. Res. Appl.*, vol. 26, no. 11, pp. 894–900, Nov. 2018.